



**HAL**  
open science

## **FraC: A new conforming mesh method for discrete fracture networks**

André Fournon, Tri-Dat Ngo, Benoit Noetinger, Christian La Borderie

► **To cite this version:**

André Fournon, Tri-Dat Ngo, Benoit Noetinger, Christian La Borderie. FraC: A new conforming mesh method for discrete fracture networks. *Journal of Computational Physics*, 2019, 376, pp.713-732. 10.1016/j.jcp.2018.10.005 . hal-01983436

**HAL Id: hal-01983436**

**<https://ifp.hal.science/hal-01983436v1>**

Submitted on 16 Jan 2019

**HAL** is a multi-disciplinary open access archive for the deposit and dissemination of scientific research documents, whether they are published or not. The documents may come from teaching and research institutions in France or abroad, or from public or private research centers.

L'archive ouverte pluridisciplinaire **HAL**, est destinée au dépôt et à la diffusion de documents scientifiques de niveau recherche, publiés ou non, émanant des établissements d'enseignement et de recherche français ou étrangers, des laboratoires publics ou privés.

# FraC: A new conforming mesh method for discrete fracture networks

André Fournou<sup>1\*</sup>, Tri-Dat Ngo<sup>1,3</sup>, Benoit Noetinger<sup>1</sup>, Christian La Borderie<sup>2</sup>

<sup>1</sup> IFP Energies Nouvelles, 1&4 Avenue du Bois Préau 92500 Rueil-Malmaison, France.

<sup>2</sup> University of Pau & Pays Adour, Laboratoire des sciences de l'ingénieur appliquées à la mécanique et au génie électrique, SIAME EA 4581, Fédération IPRA, Allée du Parc Montaury, Anglet, France

\*Corresponding author, Tel.:+33 1 47 52 72 57. Fax: +33 1 47 52 60 31.

[andre.fournou@ifpen.fr](mailto:andre.fournou@ifpen.fr)

## Abstract

The Fracture Cut (FraC) approach to mesh three-dimensional (3D) Discrete Fracture Networks (DFN) is presented. The considered DFNs consist of a network of planar two-dimensional (2D) fractures sharing intersections that can in turn intersect themselves, resulting in highly complex meshing issues. The key idea of FraC is to decompose each fracture into a set of connected closed contours, with the original intersection traces located at the boundaries of the contours. Thus, intersection segments can be more easily accounted for when building a conforming mesh. Three distinct strategies for intersection points management are also proposed to enhance the quality of resulting meshes. Steady-state single-phase flow simulations are performed to validate the conform meshes obtained using FraC. The results from flow simulations as well as from a mesh quality analysis on a benchmark case show that a flexible AoM strategy (Adding or Moving intersection points) appears to be

<sup>3</sup> now at Socotec Power Services, 5, place des Frères Montgolfier, 78182 Saint-Quentin-en-Yvelines, France

25 the best choice to generate ready-to-run meshes for complex DFN. This approach also allows  
26 accounting for tiny features within the fracture networks while keeping a good mesh quality  
27 and respecting DFN connectivity. Finally, a scalability of the mesh generator is conducted to  
28 assess the performance of the approach.

29

30 **Keywords**

31 3D discrete fracture network; Mesh generation; Conforming mesh; Mesh quality; Steady-state  
32 single phase flow.

33

34

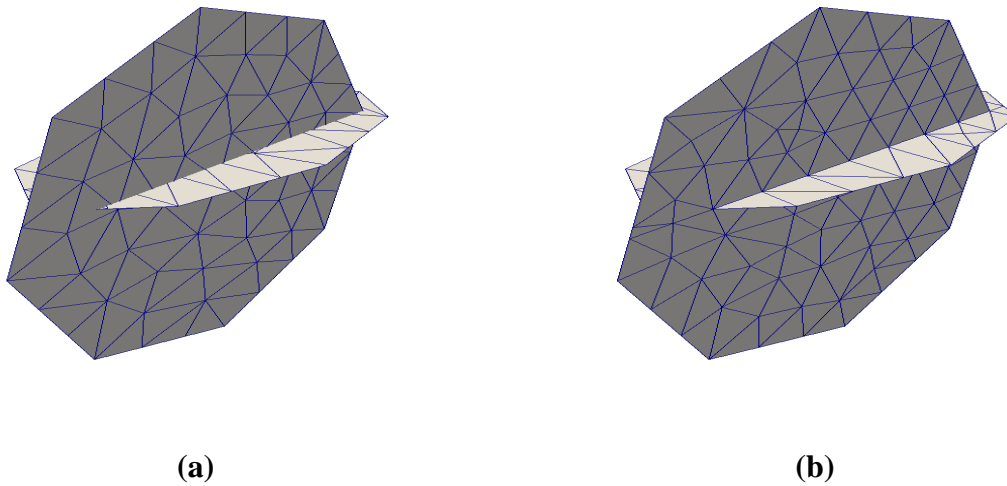
## 35 **1. Introduction**

36 Transfers in fractured porous media modeling is still a challenging issue having a broad  
37 variety of applications ranging from geothermal energy recovery (Aquilina et al., 1998),  
38 petroleum exploration and production (Bourbiaux, 2010), CO<sub>2</sub> geological storage to nuclear  
39 waste disposal (Grenier et al., 2005). Fracture networks may be studied using either  
40 continuous (Svensson, 2001; Karimi-Fard et al., 2006; Fournon et al., 2007) or Discrete  
41 Fracture Networks (DFN) models (Erhel et al., 2009; Hyman et al., 2014; Delorme et al.,  
42 2016; Ricois et al., 2016; Berrone et al., 2017). In practice, continuous models may be used  
43 when a representative elementary volume (REV) exists, that is small compared with other  
44 characteristic sizes of the problem (Long et al., 1982; Neuman, 1988). At this scale transfers  
45 in fractured media may be modeled using volumetric grids with equivalent properties that  
46 mimic the properties of the underlying DFN. Numerous works deal with the effective  
47 computation of equivalent properties (Karimi-Fard et al., 2006; Matthai and Nick, 2009;  
48 Fournon et al., 2013, Jourdain et al., 2014). Another common approach may be followed,  
49 especially if no REV exists or in order to obtain high-resolution simulations. In this approach  
50 the DFN geometry is explicitly accounted for. With recent advances coming from  
51 continuously growing computing power and with widespread research efforts of the  
52 community to build detailed meshes as well as adapted numerical schemes, transfers can be  
53 modeled on more and more complex explicit DFN geometries.

54 To our knowledge, three distinct discrete approaches are used to obtain numerical flow and  
55 transport simulations on DFN meshes. The first approach, so-called pipe-network models (or  
56 capacitor/resistor models, Acuna and Yortsos, 1991, Bodin et al., 2007), assumes that the flow  
57 is channelized within the network and models fracture connections as one-dimensional  
58 channels. The final model is a linear system involving a set of porous volumes and

59 conductivities coupling fracture intersections that share common fractures. Using this strong  
60 topological simplification, the overall connectivity between fractures is maintained and the  
61 computational cost is significantly reduced because internal degrees of freedom inside each  
62 fracture are neglected. These approaches have been used long ago for steady-state flow and  
63 transport (Cacas et al., 1990; Dershowitz and Fidelibus, 1999; Gylling et al., 1999). More  
64 recently, Noetinger and Jarrige (2012) have proposed a systematic approach for mapping 3D  
65 DFN to pipe networks considering transient Darcy flow in complex 3D fractured networks  
66 only. This work was later extended to account for transfers arising from the matrix  
67 (Noetinger, 2015). Local transport properties of pipe networks models can be determined  
68 analytically via simple estimations (Cacas et al., 1990) or numerically using direct local  
69 calculations that can involve fine meshing of each fracture (Noetinger and Jarrige 2012). The  
70 fine meshing can be avoided using simplifying assumptions (Khvoenkova and Delorme,  
71 2011) that are in between the approach of Cacas et al (1990) and Noetinger and Jarrige  
72 (2012).

73 The two other alternative approaches keep the exact geometry of DFN considering that  
74 fractures are modeled as planar objects. The second approach proposes to use non-conforming  
75 meshes in order to alleviate meshing difficulties due to the occurrence of multi-intersections  
76 (Fig. 1a).



77 *Fig. 1. Non-conforming (a) and conforming mesh (b) for a two-fracture system.*

78 However, in order to handle these non-conforming meshes, advanced numerical schemes are  
 79 required, so specific codes have to be developed, and one cannot use existing platforms  
 80 without deep modifications of the codes. We may refer to the PDE-constrained optimization  
 81 approach (Berrone et al., 2013; Benedetto et al., 2014, 2016; Berrone et al., 2017) and the  
 82 Mortar method (Erhel et al., 2009; Pichot et al., 2010, 2012).

83 The third approach is to develop tools allowing to build conform mesh. This is the approach  
 84 developed in the present paper (Fig. 1b). The main idea is that major workload will be spent  
 85 on generating DFN meshes rather than in the development of specific numerical approaches  
 86 (Adler et al. 2012). Recent studies dealt with conform mesh approaches (Hyman et al., 2014,  
 87 2015; Huang et al., 2016; Fournon et al., 2016; Ngo et al. 2017). CPU time for DFN mesh  
 88 generation may be considerably reduced in line with progress in computer sciences and  
 89 information technology. In addition, beside the geometrical DFN meshing difficulties, a  
 90 second issue relates to the “non-manifold” topology of the resulting meshes (Sander et al.,  
 91 2015). This particular issue can be handled by several finite element codes such as Cast3M  
 92 (2017). For instance, Fournon et al. (2016) provided numerical solutions for steady-state  
 93 single-phase flow on non-manifold meshes by means of the Finite Element (FE) or Mixed  
 94 Hybrid Finite Element (MHFE) methods implemented in Cast3M (2017). Few finite volume

95 simulators for subsurface flow and transport, like PFLOTRAN (Lichtner et al., 2013;  
96 Hammond et al., 2014; Hyman et al., 2014; Makedonska et al., 2015; Karra et al., 2015;  
97 Hyman et al., 2015) and DuMux (Huber et al., 2000, Flemisch et al., 2011), are also able to  
98 deal with non-manifold topologies.

99 In all cases, the mesh generation remains a crucial bottleneck because the convergence and  
100 stability of the numerical scheme as well as the solution accuracy could be significantly  
101 affected by the mesh quality. In principle, degenerate cells that do not satisfy the quality  
102 constraints should be identified and removed from the final mesh. Botsch and Kobbelt (2001)  
103 classified degenerate triangles as caps, i.e. triangles with an angle close to  $180^\circ$ , and needles  
104 of which the longest edges is much longer than the shortest one. Frey and George (2000)  
105 present an overview of quality mesh measures, mainly based on the edge length or triangle  
106 angle criteria. As an example, Miller et al. (1995) and Shewchuk (1997) use the ratio of the  
107 circumscribed circle radius to the shortest edge of a triangle for judging the mesh quality. This  
108 ratio should be as small as possible for all triangles. More recently, Mustapha and  
109 Dimitrakopoulos (2011) evaluate the triangle quality by comparing its area with that of  
110 equilateral triangles. This last measure is retained for reviewing the quality of our meshes.

111

112 The present study focuses on mesh generation for complex discrete fracture network only.  
113 The matrix surrounding the fractures is disregarded. We first propose a new conforming mesh  
114 approach, so-called FraC (Fracture Cut mesh approach) and then provide validations via flow  
115 simulations done on DFN of increasingly complex geometries. The contribution is organized  
116 as follows. The methodology of the FraC approach used to obtain conforming meshes for  
117 DFN is described in Section [2](#), accompanied by a discussion on the quality of resulting  
118 meshes. Numerical results of steady-state flow on FraC meshes are shown in Section [3](#), both  
119 for model validation and demonstration purposes. In Section [4](#), scalability of the mesh

120 generator is discussed and finally, Section [5](#) gives conclusions together with some comments  
121 on further works.  
122

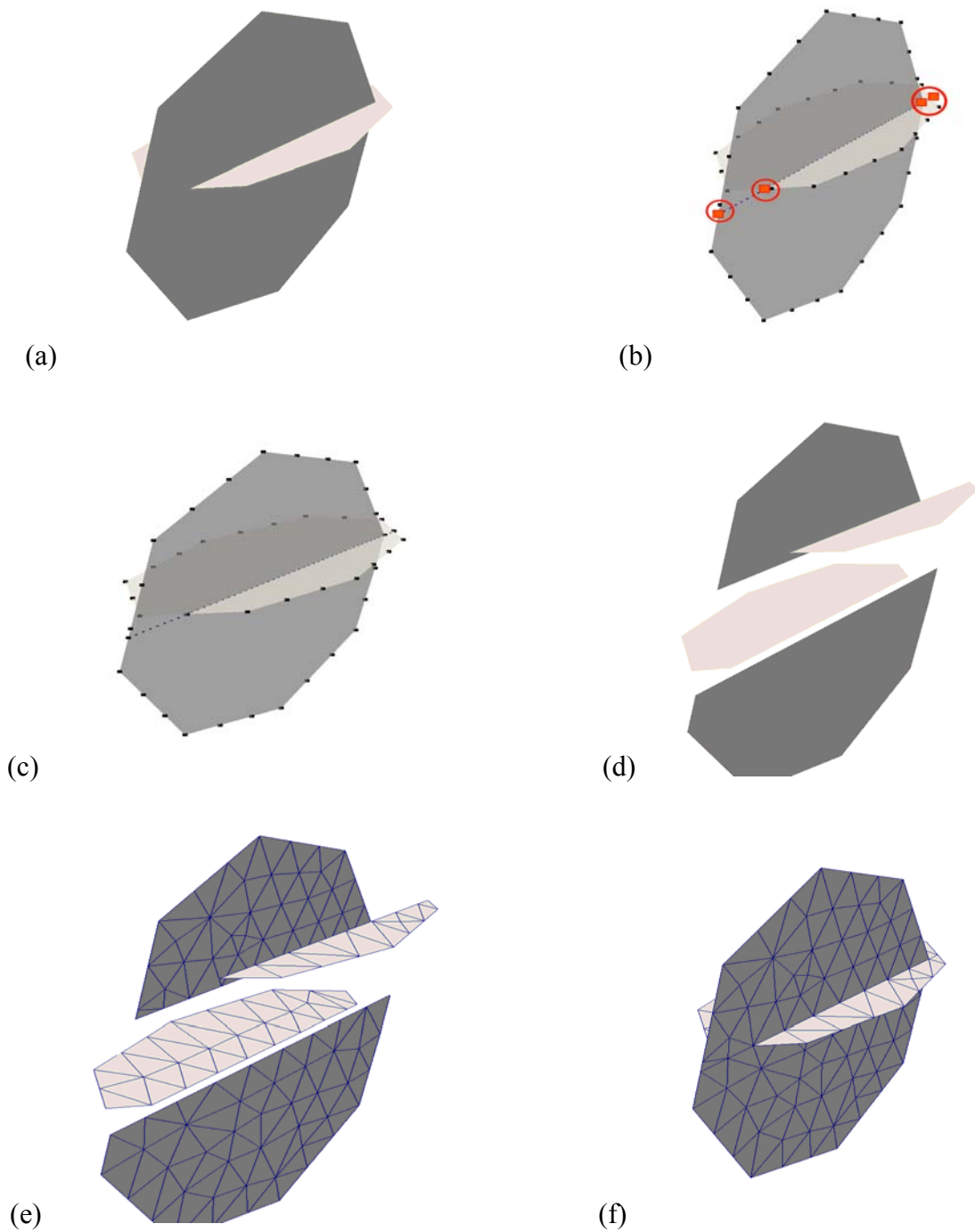
## 123 **2. FraC meshing method**

124 In fractured media, the input of mesh tools comes generally from the fractured site  
125 characterization. The site characterization provides the distribution of orientations,  
126 dimensions, and spatial locations of different fracture sets. Using these distributions DFNs are  
127 modeled. The obtained DFN are often complex and their fractures may be concave polygons  
128 or ellipses. To model transfers in the DFN, we choose to build a dedicated mesh of the DFN  
129 geometry. Unlike Hyman et al. (2014) who developed a feature rejection algorithm for  
130 meshing (FRAM) before generating DFN conforming grids we propose to deal with all the  
131 DFN fractures ensuring the DFN connectivity conservation. Hereby we propose a simple and  
132 efficient meshing approach for DFNs, the so-called “Fracture Cut Method for Meshing”  
133 (FraC).

134 The main idea of the FraC approach is to decompose each fracture into a set of connected  
135 closed contours, between which common segments will be discretized in a conforming  
136 manner. Strategies for moving or adding intersecting points are applied in order to achieve an  
137 acceptable quality of the final mesh.

### 138 **2.1. General theoretical background**

139 The FraC method involves three primary stages. Considering two intersecting fractures  
140 (Fig. 2a.), the meshing procedure is as follows: ( $S_1$ ) contour meshing (Fig. 2b, black points)  
141 and fracture intersection identification (Fig. 2b, orange points); ( $S_2$ ) intersection point  
142 management (Fig. 2b, inside the red circles) to obtain the final contour meshing (Fig. 2c) and  
143 fracture cutting (Fig. 2d), and ( $S_3$ ) triangulation (Fig. 2e) and merging triangulated surfaces  
144 (Fig. 2f). The main features in each stage are summarized below.



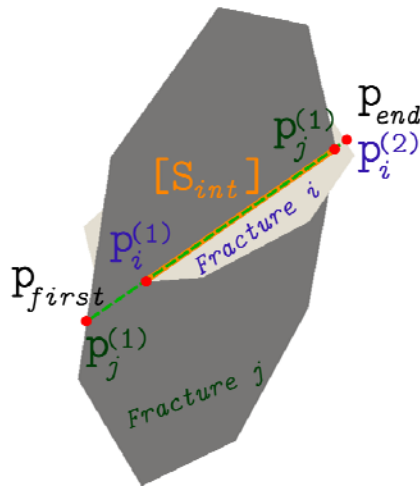
145

146 *Fig. 2. Illustration of a 2-fracture DFN (a). Meshing procedure: step  $S_1$  – fracture contour*  
 147 *discretization (black points) and intersection points (orange points) identification (b); step  $S_2$*   
 148 *– intersection point managements (inside red circles) (b) and final contour discretization (c).*  
 149 *Exploded view of fracture cutting results (d); and step  $S_3$  – exploded view of the contour*  
 150 *triangulation results (e) and merging triangulated surfaces (f).*

151 2.1.1. Contour discretizing and fracture intersection identification

152 The fracture shapes in our DFN are planar ellipses or convex planar polygons. Elliptic  
153 fractures are defined by a center point, the minor and major axe lengths and a normal vector.  
154 Polygon fractures are defined by points. Firstly a characteristic length  $h_i$  is chosen for each  
155 fracture. This characteristic length is used to discretize the fracture contour and is respected  
156 wherever it is possible during the DFN meshing. It means that the edge lengths of the final  
157 mesh triangles will be of the same order of magnitude as  $h_i$ . At this step, the fractures are thus  
158 modeled as convex polygons  $F_i$ . The representative polygons  $F_i$  of elliptic fractures are  
159 inscribed in the fracture shapes that underestimates the fracture surface and possibly the  
160 intersection between fractures. Therefore, the characteristic length  $h_i$  has to be carefully  
161 chosen, too high values could lead to the loss of fracture connectivity, too small values results  
162 in a high mesh cell number. Moreover,  $h_i$  should not be too different between fractures to  
163 avoid creating elongated low-quality mesh cells around the intersection location between  
164 these fractures. Obviously, the choice of  $h_i$  has no impact on DFN geometry if only polygonal  
165 fractures belong to the DFN. The next step involves finding intersections between the  
166 polygons. At this stage, an octree-like approach (Khvoenkova and Delorme, 2011; Hyman et  
167 al., 2014) is used to improve the computational efficiency. This approach works well if the  
168 size of the fractures is almost of the same order of magnitude (Ngo et al., 2017). First, an axis-  
169 aligned minimum bounding box  $BB_i$  is created around  $F_i$  where  $BB_i$  is defined by the  
170 minimal and maximal value of the corresponding coordinate of the polygon vertices. Then a  
171 preliminary test is performed to check the intersection between the bounding boxes  $BB_i$  and  
172  $BB_j$  of two fractures  $F_i$  and  $F_j$  respectively. Obviously, the intersection between  $F_i$  and  
173  $F_j$  occurs only if  $BB_i$  and  $BB_j$  do intersect. In this case, an intersection line  $]L_{ij}[$  between the  
174  $F_i$  and  $F_j$  planes is first determined. Let  $\partial F_i$  be the boundary of  $F_i$ , then finding

175 intersections between the fractures becomes finding intersections between  $\partial F_i$ ,  $\partial F_j$  with  
176  $]L_{ij}[$ . We denote  $n_{ij}^{(\alpha)}$  the number of intersection points between  $\partial F_i$  and  $\partial F_j$  with  $]L_{ij}[$ .  
177 Considering the most general cases, four intersection points  $\mathbf{p}_i^{(1)}, \mathbf{p}_i^{(2)}, \mathbf{p}_j^{(1)}, \mathbf{p}_j^{(2)}$  ( $n_{ij}^{(i)} = n_{ij}^{(j)} = 2$ )  
178 may therefore be found, where  $\mathbf{p}_i^{(1,2)}$  lie on  $F_i$  and  $\mathbf{p}_j^{(1,2)}$  lie on  $F_j$ . We can notice that these  
179 points may coincide and that each one belongs at least to a fracture contour. Finally, the  
180 fractures intersect only if  $[\mathbf{p}_i^1 \mathbf{p}_i^2] \cap [\mathbf{p}_j^1 \mathbf{p}_j^2] \neq \emptyset$ . The intersection points are then sorted to find  
181 out the endpoints, mentioned as  $\mathbf{p}_{first}$  and  $\mathbf{p}_{end}$ . An extended intersection segment  $[\mathbf{p}_{first} \mathbf{p}_{end}]$   
182 is built to connect the intersection endpoints belonging to the fractures  $F_i$  and  $F_j$ . Let  $[S_{int}]$   
183 be the actual intersection segment between  $F_i$  and  $F_j$ . Obviously, we have  
184  $[S_{int}] \subset [\mathbf{p}_{first} \mathbf{p}_{end}]$  (Fig. 3).



185  
186 *Fig. 3. Two intersecting fractures with used notations: the extended intersection segment*  
187  $[\mathbf{p}_{first} \mathbf{p}_{end}]$  (green dashed line) and the original intersection trace  $[S_{int}]$  (orange plain line).

188 2.1.2. Intersection point management and fracture cutting

189 Once the intersection determination stage is completed, the fracture cutting step will be  
190 performed. For this purpose, special focus should be put on the intersection points between  
191 intersecting fractures as well as the points locating in their neighboring areas. Without loss of  
192 generality, we consider two intersecting fractures  $F_i$  and  $F_j$ , each of which is modeled by a  
193 set of vertices  $V_\alpha$  with  $\alpha \in \{i, j\}$ . The case of multi-intersection could be treated similarly  
194 and will be briefly addressed.

195 2.1.2.1. *Intersection point management*

196 This paragraph describes the strategies for intersection point management to  
197 discretize each fracture contour  $\partial F_i$ . Let  $\mathbf{p}$  be one of the four intersection point between  $F_i$   
198 and  $F_j$ . Three strategies may be applied for the intersection point management:

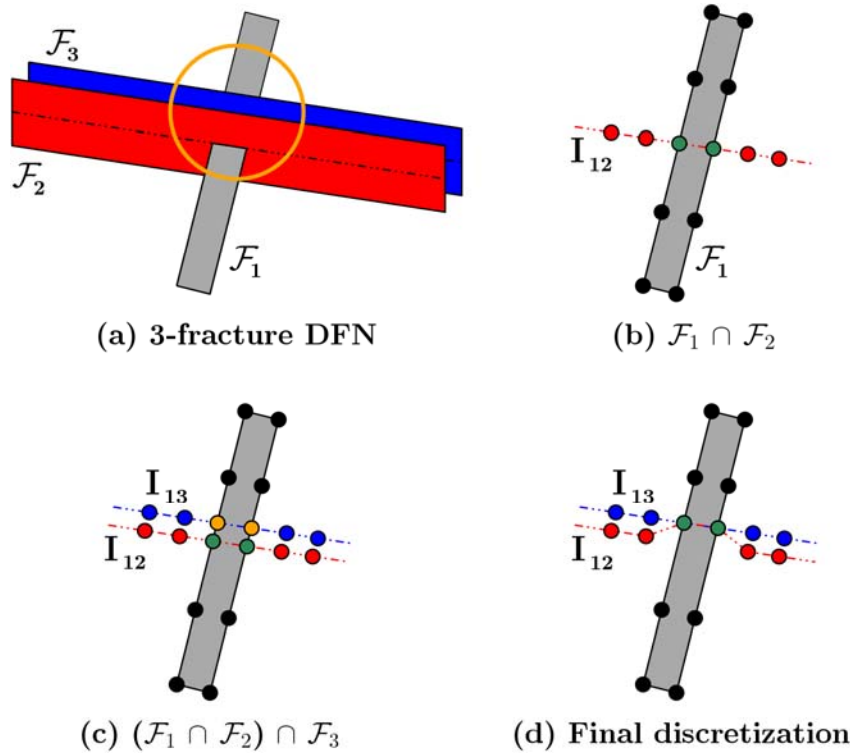
199 a. Always Add (AA) intersection points

200 Disregarding the position of neighboring points, intersection points are always added to the  
201 fracture contours to which it belongs. However using this strategy extremely small edges and  
202 consequently poor-quality elements with very high aspect ratio could appear in the final DFN  
203 mesh.

204 b. Always Move (AM) closest points

205 Two points (each point belongs to one of intersecting fractures,  $\overline{\mathbf{p}}_i \in F_i$  and  $\overline{\mathbf{p}}_j \in F_j$ ) which  
206 are closest to the intersection point  $\mathbf{p}$  are identified. These points are then be merged with  $\mathbf{p}$ .  
207 The advantage of this strategy is that it avoids creating tiny edges within each sub-fractures  
208 and therefore enhance the quality of the final mesh. Nevertheless, by moving systematically  
209 contour points, the fracture geometries are deformed and may no longer be planar. An  
210 example is given in Fig. 4 considering a 3-fracture system. As fracture intersections are

211 handled sequentially, the process of moving contour points leads to the deformation the  
 212 vertical fracture  $F_2$ .



213 (a) 3-fracture DFN (b)  $\mathcal{F}_1 \cap \mathcal{F}_2$   
 214 (c)  $(\mathcal{F}_1 \cap \mathcal{F}_2) \cap \mathcal{F}_3$  (d) Final discretization

214 Fig. 4. 3D example showing how a fracture shape may be modified when moving contour  
 215 points to intersection points. a) 3-fracture system consisting of two vertical fractures,  $F_2$  (in  
 216 red) and  $F_3$  (in blue), intersected by a horizontal one  $F_1$ ; b) Discretization of the  $F_1$  contour  
 217 (black points) and the intersection between  $F_1$  and  $F_1$  ( $I_{12}$ ), the two intersection points are in  
 218 green; c)  $F_3$  is now accounted for in the DFN, intersection line ( $I_{13}$ ) and points (in orange)  
 219 are determined; d) the green points on  $I_{12}$  are moved to the orange ones, resulting in  
 220 deformation of  $I_{12}$  and consequently  $F_2$  is no longer planar.

221  
 222 More harshly, in some cases it could lead to the loss of connectivity of the fractures if other  
 223 intersection points locate within a deformation area. All of that could have important effects  
 224 on flow simulations.

225 c. Add or Move (AoM) points

226 Based on a flexible moving and adding point strategies, an adaptive solution is proposed. A  
227 critical length  $L_{min}$  is determined basing on the characteristic length of  $h_i$  and  $h_j$ . Concretely,  
228  $L_{min} = \max\{\varepsilon_h \cdot h_i, \varepsilon_h \cdot h_j\}$  where  $\varepsilon_h$  is a user-defined ratio,  $0 < \varepsilon_h < 0.5$ . When  $\varepsilon_h$  is too small  
229 (close to 0) or too high ( $\sim 0.5h$ ), the resulting mesh is very similar to the one obtained using  
230 the AA and the AM approach, respectively. From our experiences,  $\varepsilon_h=0.2$  seems to be a good  
231 choice. As in the AM approach, the two closest points to the intersection  $\overline{\mathbf{p}_\alpha}$  ( $\alpha \in \{i, j\}$ ) are  
232 determined. Then,  $\overline{\mathbf{p}_\alpha}$  is removed if the distance from  $\overline{\mathbf{p}_\alpha}$  to  $\mathbf{p}$  is less than  $L_{min}$ . In any case,  
233  $\mathbf{p}$  is added to the vertex set of each contour. Locally the characteristic length of the contour is  
234 thus modified but remains close to  $h_\alpha$  around the contour. This approach allows to remove  
235 tiny edges from the final mesh on the one hand and to limit the deformation of the fractures  
236 on the other hand. We may also notice that for all strategies intersection point positions are  
237 conserved. Thanks to that the following step will be easier to manage. The choice of the  
238 strategy for the intersection point management will be further discussed in Sections 2.2 and  
239 3.1.

240 2.1.2.2. *Fracture cutting*

241 The fracture cutting step expresses the key idea of the FraC approach and is solely  
242 applied for intersecting fractures. Each of two intersecting fractures  $F_i$  and  $F_j$  is then cut  
243 along the extended intersection  $[\mathbf{p}_{first} \mathbf{p}_{end}]$  to obtain interconnected closed contours,  
244 subsequently referred to as “sub-fractures”. To guarantee the homogeneity of the final mesh,  
245 the extended intersection segment  $[\mathbf{p}_{first} \mathbf{p}_{end}]$  should also be discretized according to the  
246 mesh characteristic length of the two original fractures. For that, special focus is put on

247  $[\mathbf{p}_{first}\mathbf{p}_{end}]$  which can also be sub-divided in a homogeneous or adaptive manner while  
 248 keeping all intersection points unchanged. In the first case a target edge length  $h_{ij} = \min(h_i, h_j)$   
 249 is defined, the segments  $[\mathbf{p}_{first}\mathbf{p}_{end}] \setminus [S_{int}]$  and  $[S_{int}]$  are both discretized using  $h_{ij}$ . In the  
 250 second case, only  $[S_{int}]$  is discretized according to  $h_{ij}$ , the extended segment  $[\mathbf{p}_{first}\mathbf{p}_{end}] \setminus [S_{int}]$   
 251 is discretized using  $h_i$  or  $h_j$ , depending if it belongs to  $F_i$  or  $F_j$  respectively.  
 252 Finally, by a series of cutting steps, the original fractures are decomposed into a large number  
 253 of connected closed contours. The main benefit of series of cutting steps is that multiple-  
 254 intersection issues vanish. For example, a problem of triple intersections between three  
 255 fractures  $F_i$ ,  $F_j$  and  $F_k$  is transformed to the standard problem of finding intersections  
 256 between  $F_k$  and the sub-fractures of  $F_i$  and  $F_j$ . The drawback of this strategy is that it  
 257 increases the number of intersection tests and, consequently, the computational time  
 258 especially when working on densely-distributed large-scale DFNs. The influence of this  
 259 feature of the method is addressed in Section 4.

### 260 2.1.3. Contour triangulation and triangulate surface merging

261 Surface triangulation is a common topic in mathematics and computational geometry  
 262 (Frey and George, 2000). Among many triangulation techniques, the Delaunay triangulation  
 263 is one of the most popular and the most often used approach (Delaunay, 1934; Bourouchaki  
 264 and George, 1998). In our framework, this classical approach is applied to each sub-fracture  
 265 according to its own target edge length  $h_i$ . To guarantee the conformity of the final mesh, no  
 266 extra node is created on the boundaries of the sub-fracture. On the other hand, nodes are  
 267 added inside the domain limited by sub-fracture boundaries, they are also constrainedly  
 268 managed allowing to improve the quality of triangles. Finally, all resulting triangulated sub-  
 269 fractures are merged into a single triangulation data structure, in which duplicate vertices

270 along the intersection lines may exist. These duplicates are then detected and removed,  
271 resulting in a final fully connected mesh. The triangulation step and the triangulated fracture  
272 merging are done using either LaGrit open source libraries (Los Alamos Grid Toolbox, 2013)  
273 or Cast3M tools (Murphy et al., 2001, Hyman et al., 2014, Cast3M, 2017).

#### 274 2.1.4. Discussion on precision parameters

275 Numerical calculations are performed in 3D. A main precision parameter,  $\epsilon_{\text{merge}}$ , is used  
276 for geometric calculations including finding the distance between two points, vector  
277 calculations and intersection point identifications. This parameter is also used to remove  
278 duplicate points, i.e. points between which the distance is less than  $\epsilon_{\text{merge}}$  will be merged.  
279 Another parameter,  $\epsilon_{\text{surf}}$ , is used to remove tiny contours whose surfaces are smaller than  $\epsilon_{\text{surf}}$ .  
280 This parameter is very useful when considering the AA approach in which small contours  
281 may frequently be created, especially around multiple intersection locations. All removed  
282 contours are marked during the meshing step to be validated by user afterward. These two  
283 precision parameters are chosen accordingly to  $L_{\text{min}}$ . In the following sections,  $\epsilon_{\text{merge}} = L_{\text{min}} \times$   
284  $10^{-4}$  and  $\epsilon_{\text{surf}} = L_{\text{min}}^2 \times 10^{-2}$ .

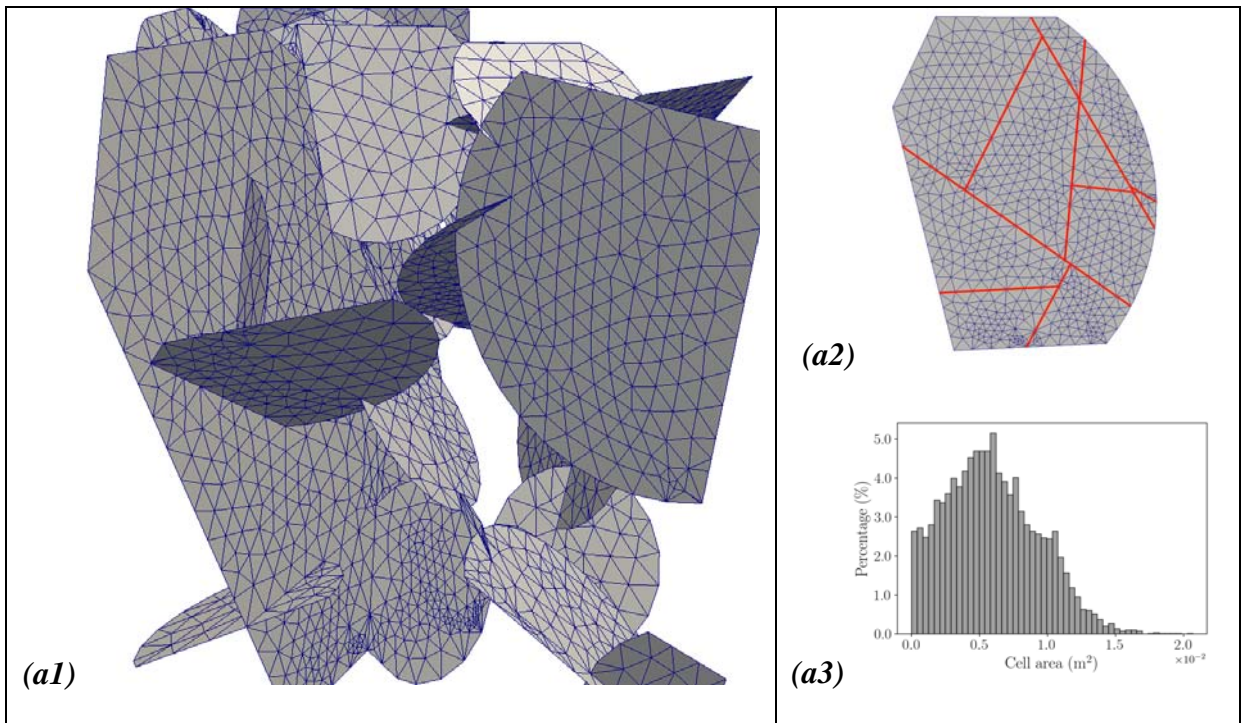
#### 285 2.2. Discussion on mesh quality

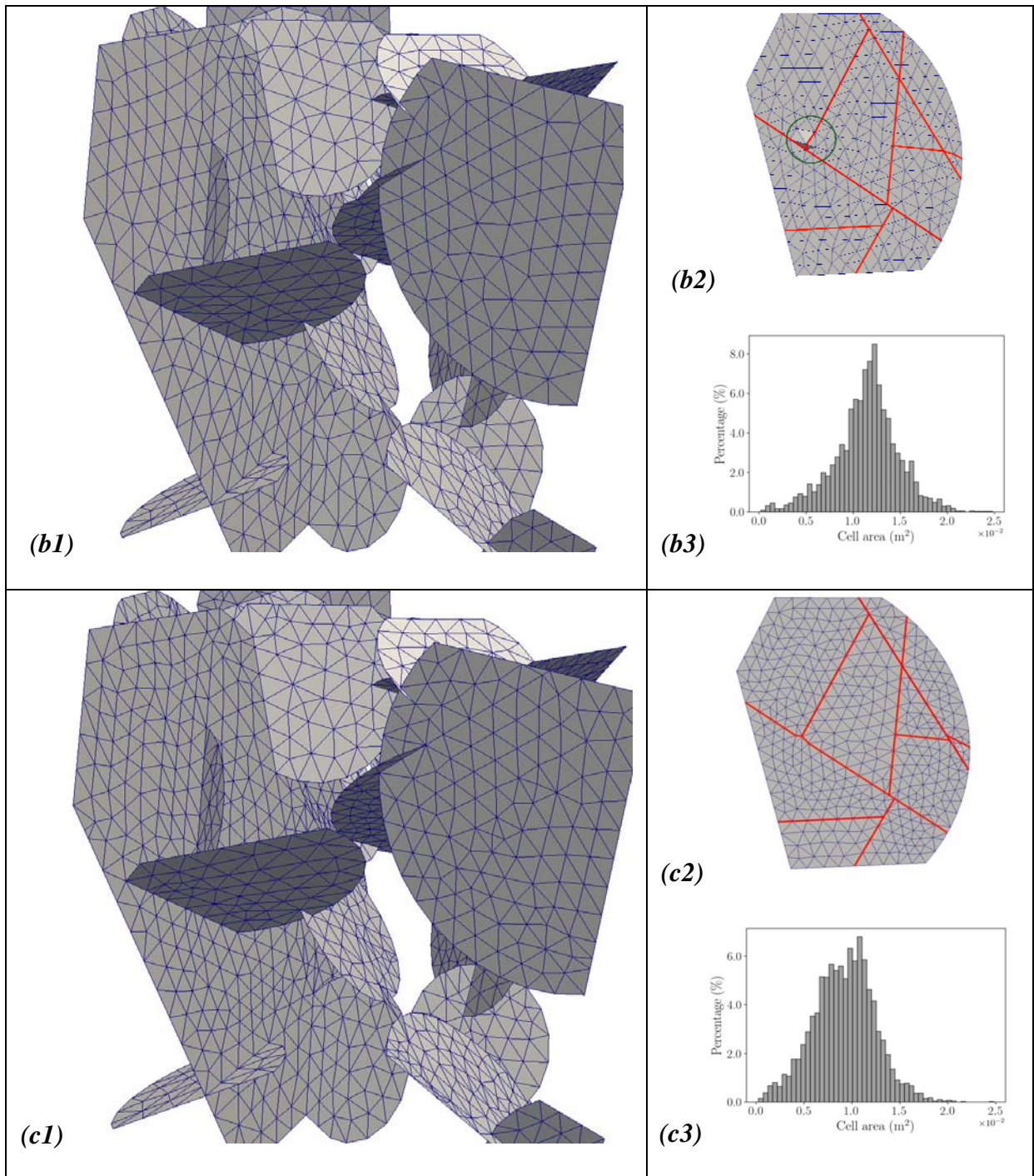
286 In this section, we consider a synthetic DFN, which was also studied by a number of  
287 authors (e.g. Khvoenkova and Delorme, 2011; Delorme et al., 2016; Ngo et al., 2017). The  
288 network consists of 33 dish-shaped fractures inside a  $3\text{m} \times 3\text{m} \times 3\text{m}$  cube. All three  
289 intersection strategies (i.e. AA, AM and AoM approach) are used for the mesh generation of  
290 this DFN. A common characteristic length  $h$  is set for all fractures. Several meshing  
291 realizations are performed with decreasing  $h$  to obtain a set of meshes with different levels of  
292 refinement. The characteristic length  $h$  is chosen from 1.0 m to  $3.75 \times 10^{-3}$  m resulting in grids  
293 that contains from  $2 \times 10^2$  to  $8.0 \times 10^6$  elements.

294 Fig. 5 (a1,b1,c1) shows the meshes generated using AA approach (Fig. 5a1), AM approach  
295 (Fig. 5b1) and AoM approach (Fig. 5c1) with the characteristic length  $h$  being about 0.12 m.  
296 Fractures within this synthetic DFN are divided into 157 closed contours. The resulting  
297 meshes contain about  $2 \times 10^3$  mesh cells. The final triangulation of the largest fracture within  
298 the DFN are plotted in Fig. 5 (a2, b2, c2) . Fig. 5 (a3, b3, c3) display the histograms of the  
299 mesh cell area of the resulting meshes.

300

301





302 Fig. 5. Examples of meshes generated using AA (a1), AM (b1) and AoM (c1) approaches and  
 303 associated histograms of the mesh cell area (Figs a3, b3, c3). Figures a2, b2, c2 present the  
 304 final triangulation of the largest fracture. The red bold lines illustrate the extended  
 305 intersection traces.

306

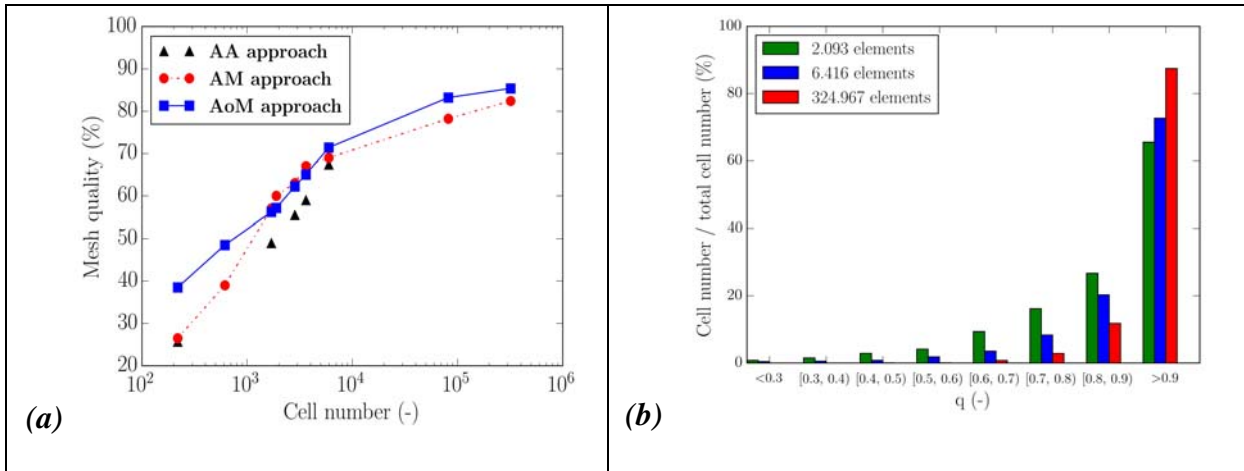
307 The mesh in Fig. 5a1 and Fig. 5a2 reveals several drawbacks of the AA approach. First, one  
308 can easily observe that this mesh is not homogeneous, there exists locally mesh cells of which  
309 the edge size is of different order of magnitude. It can also be observed in Fig. 5a3 that the  
310 AA mesh contains a large amount of tiny features (i.e. mesh area close to zero). The  
311 difference in size of mesh cells can amplify numerical diffusion as well as convergence  
312 difficulties, and therefore can affect significantly the result of flow and transport simulations.  
313 Second, as mentioned above in Section 2.1, when using the AA approach, the triangulation of  
314 close contours can fail due to the appearance of extremely close points in the vertex set of  
315 sub-fractures.

316 Fig. 5b1 displays the mesh created by FraC using the AM approach for intersection point  
317 treatment. This mesh is much more homogeneous in terms of mesh size than the AA mesh  
318 (Fig. 5b3). However, the non-planarity of fractures is noticeable (Fig. 5b2). For instance, it  
319 shows the contrast in color between some neighboring mesh cells inside the circle, implying  
320 that these cells do not lie on a same plane. Furthermore, the mesh generated using the AoM  
321 approach is less deformed compared to the AM mesh (uniform color are observed by fracture  
322 planes in Fig. 5c2), while keeping a good mesh homogeneity (Fig. 5c3).

323 A cell aspect ratio,  $q = 4\sqrt{3} \frac{A}{\sum_{i=1}^3 s_i}$ , where A is the triangle area and  $s_i$  is the length of the side

324  $i$  (Mustapha and Dimitrakopoulos, 2011) is now used to assess the mesh quality. Fig. 6a  
325 depicts the percentage of mesh cell having a good aspect ratio within the resulting meshes.

326



327 Fig. 6. Mesh quality of resulting meshes. a) Global mesh quality as a function of number of  
 328 mesh cells. b) Quality histogram for three realizations using the AoM approach.

329

330 It shows missing data on the AA curve because of meshing failure, especially for very low or  
 331 very high  $h$  values (Fig. 6a). Moreover, the quality of the AM and AoM meshes are similar, in  
 332 particular for moderate numbers of grid cells. Nevertheless the AoM approach gives better  
 333 mesh quality than the AM one for the fine meshes containing more than  $10^4$  elements.

334 In a word, the AoM approach seems to be the best choice that is able to deliver ready-to-run  
 335 meshes of good quality. As some mesh contour points may be moved, the characteristic  
 336 length of the contour may be modified locally within the intersection area. Therefore, cells  
 337 with lower quality may appear close to the intersection lines. Nevertheless, the cell quality  
 338 stay above 60% even for coarse meshes (Fig. 6b). Additional studies are given in Appendix A  
 339 to illustrate how the FraC approach deals with bounded fractures, multiple intersections as  
 340 well as to assess the influence of  $L_{\min}$  parameter on resulting meshes. In the next section, the  
 341 FraC meshes will be used as inputs of steady-state flow simulations and validated against  
 342 available benchmark simulation results and analytical solutions.

343

### 344 **3. Mesh validation by steady-state single-phase simulations**

345 As mentioned above, FraC meshes may be used as input for Cast3M (2017) or Dumux  
346 (2017). In order to validate the meshing approach, three test-case simulations are conducted:  
347 the two first validations are done using Cast3M (finite element numerical scheme) whereas  
348 the last one using Dumux (finite volume numerical scheme). The mesh validation using  
349 single-phase flow simulations are performed by considering the effective permeabilities along  
350 three main directions of the DFN block. A Dirichlet-condition for pressures is specified on  
351 two opposite facets  $\Gamma_i$  and  $\Gamma'_i$  of the domain, leading to a directional pressure gradient  $\Delta P_i$ .  
352 No-flow conditions are prescribed on the other boundaries. The effective permeabilities may  
353 then be calculated using the inverted Darcy equation based on the pressure gradient and the  
354 normal fluxes computed on  $\Gamma_i$  or  $\Gamma'_i$  (Zimmerman et al., 1996). Although this classical  
355 upscaling approach is not consistent to determine upscaled properties of highly heterogeneous  
356 media, it is still useful for validation purposes.

357

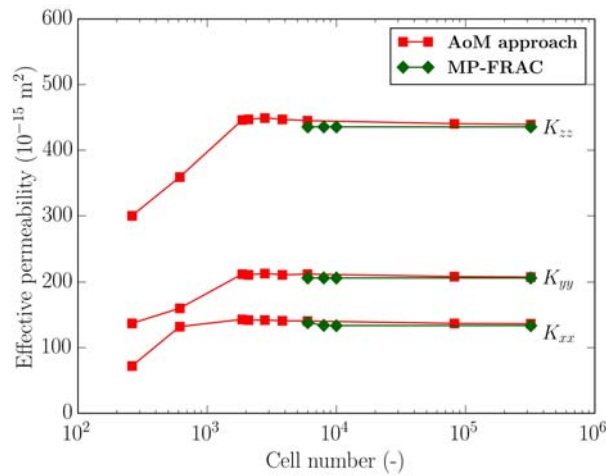
#### 358 **3.1. Benchmark simulations**

359 The benchmark simulations are performed on the previous 33-fracture network previously  
360 studied in Section 2.2. We consider the meshes created using the AoM approach to assess the  
361 effect of the strategy for intersection points management.

362 Fig. 7 shows the effective permeabilities along three main directions  $x$ ,  $y$ ,  $z$  computed from  
363 single-phase flow simulations on FraC meshes, which are then compared to the solution of the  
364 MP-Frac code (De Dreuzy et al., 2013).

365 The MP-Frac meshing approach is based on a discretization of the intersections using a 3D  
366 regular grid. This stair discretization are projected onto fracture planes and local adjustments  
367 are done to guarantee the geometrical properties (Erhel et al., 2009a; Pichot et al., 2012;  
368 Pichot et al., 2010). In the FraC approach, no regular grid or projections are used.

369 Nevertheless, as already explained, the critical point is how to deal with the intersection  
370 points.



371  
372 *Fig. 7. Effective permeabilities computed from flow simulations on our meshes and the*  
373 *solution obtained through the MP-Frac code (De Dreuzy et al., 2013).*

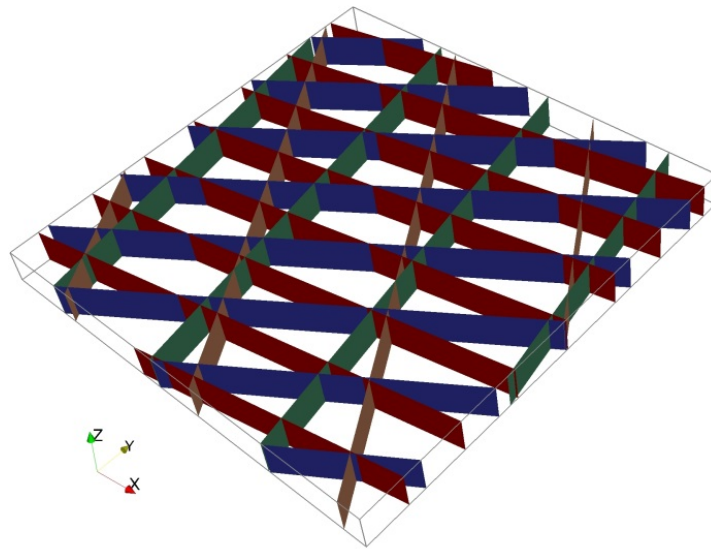
374  
375 The underestimated effective permeabilities are observed from very coarse simulations on  
376 AoM meshes. This is however an expected result. Indeed, for high  $h_i$  values, the discretized  
377 contours of the fractures do not have enough points to be representative of elliptic fractures.  
378 Therefore, some fracture intersections cannot be captured, resulting in the reduced  
379 connectivity of the DFN. The underestimation of effective permeabilities are thus the direct  
380 consequence of a decrease of DFN connectivity due to the poor contour discretization.  
381 Contrariwise, simulations on fine meshes generated using the AoM approach are in excellent  
382 agreement with the MP-Frac results. This implies that the connectivity of the fracture network  
383 is well captured in these meshes. Furthermore, by limiting the displacement of points and  
384 consequently the deformation of fractures, the AoM approach is able to alleviate the  
385 discrepancy between the computed effective permeabilities and the reference solutions.

386

387 To summarize, in light of studies on the mesh quality and the accuracy of flow numerical  
388 simulations, the AoM approach appears to be the best solution for the intersection point  
389 treatment.

### 390 **3.2. Comparison with analytical approaches**

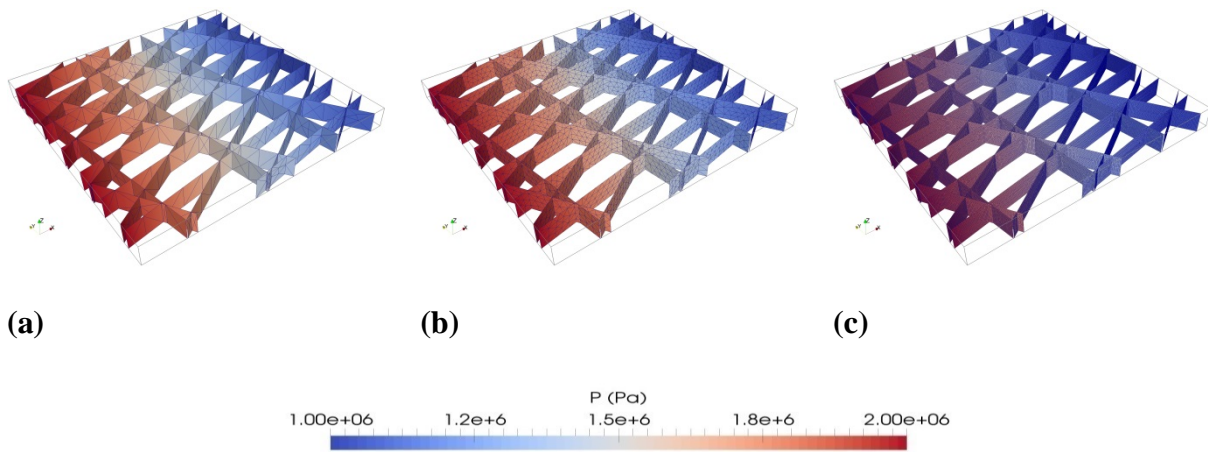
391 The fracture network studied in this section is a MWR-DFN (Modified Warren and Root  
392 DFN), which is inspired from the work of Warren and Root (1963). This DFN, already  
393 studied by Fournon et al. 2013, includes two superimposed sets of structured fractures in a  
394 100m x 100m x 8m block. Each set involves two orthogonal fracture families (Fig. 8).



395  
396 *Fig. 8. Illustration of the fracture network MWR-DFN including two superimposed sets of*  
397 *structured fractures (WR-DFNs). Each set involves two orthogonal fracture families: the red*  
398 *and green fractures belong to the first WR-DFN and the blue and orange fractures gather*  
399 *together in the second WR-DFN. We refer the readers to the online version of this paper for*  
400 *the color mentioned in this caption.*

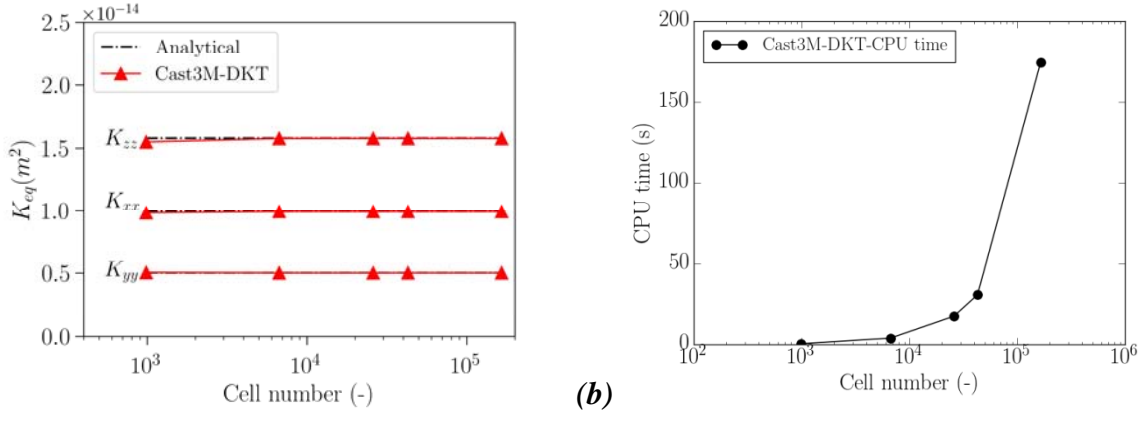
401  
402 The effective permeabilities along three principal directions of the MWR-DFN are calculated  
403 both analytically by the Oda's approach (Oda 1985) and numerically via steady-state single-  
404 phase flow simulations. Numerical simulations are run on several meshes of different levels

405 of mesh refinement. The MWR-DFN is homogeneous with the isotropic permeability of the  
 406 fractures  $k_f = 4 \times 10^{-12} \text{ m}^2$  and the fracture aperture of  $b = 2 \times 10^{-2} \text{ m}$ . Fig. 9 illustrates the  
 407 solutions of single-phase flow simulations along  $x$ -axis on three meshes of the MWR-DFN:  
 408 simulations on a very coarse mesh with  $h=5\text{m}$  (a), on a coarse mesh with  $h=1\text{m}$  (b) and on a  
 409 fine mesh with  $h=0.1\text{m}$  (c).  
 410



411 *Fig. 9. Numerical results of single-phase flow simulations along  $x$ -axis on three meshes of the*  
 412 *MR-DFN: on a very coarse mesh with  $h=7.5\text{m}$  (a), on a coarse mesh with  $h=3.0\text{m}$  (b) and on*  
 413 *a fine mesh with  $h=0.5\text{m}$  (c). These meshes contain respectively about  $1 \times 10^3$ ,  $7 \times 10^3$  and*  
 414  *$2 \times 10^5$  mesh cells.*

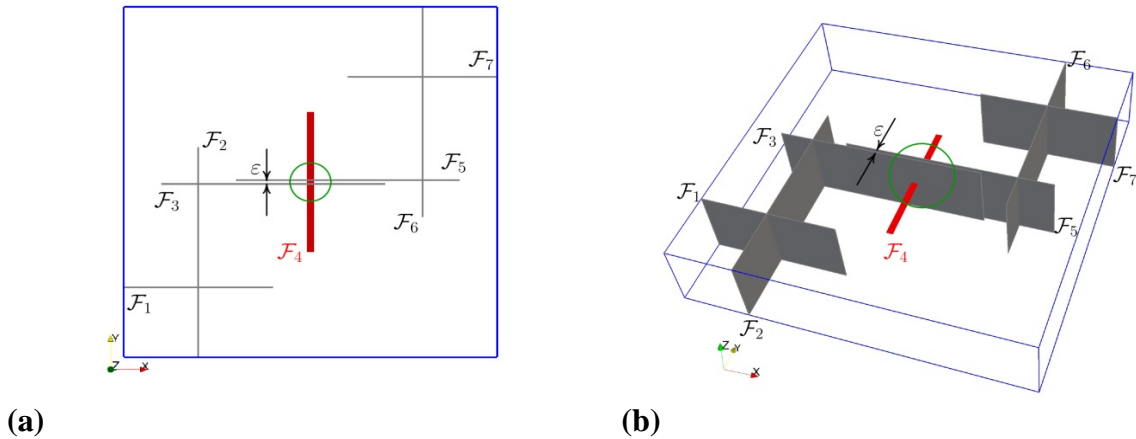
415  
 416 Fig. 10a reports a comparison between the analytical and numerical effective permeabilities  
 417 along principal directions, showing an excellent agreement between the analytical and  
 418 numerical solutions. In addition, a diagram of the computational time of simulations on  
 419 MWR-DFN meshes is displayed in Fig. 10b. The numerical simulations run very fast, for  
 420 example the simulation on the finest meshes (about  $2 \times 10^5$  mesh cells) takes only a few  
 421 minutes on a personal desktop (RAM 16Go, 8 processors Intel(R) Xeon(R) CPU E5-1620 v3  
 422 @ 3.5GHz).



423 Fig. 10. MWR-DFN: (a) Computed effective permeabilities along three principal directions  
 424 and (b) total elapsed time for mesh generation.

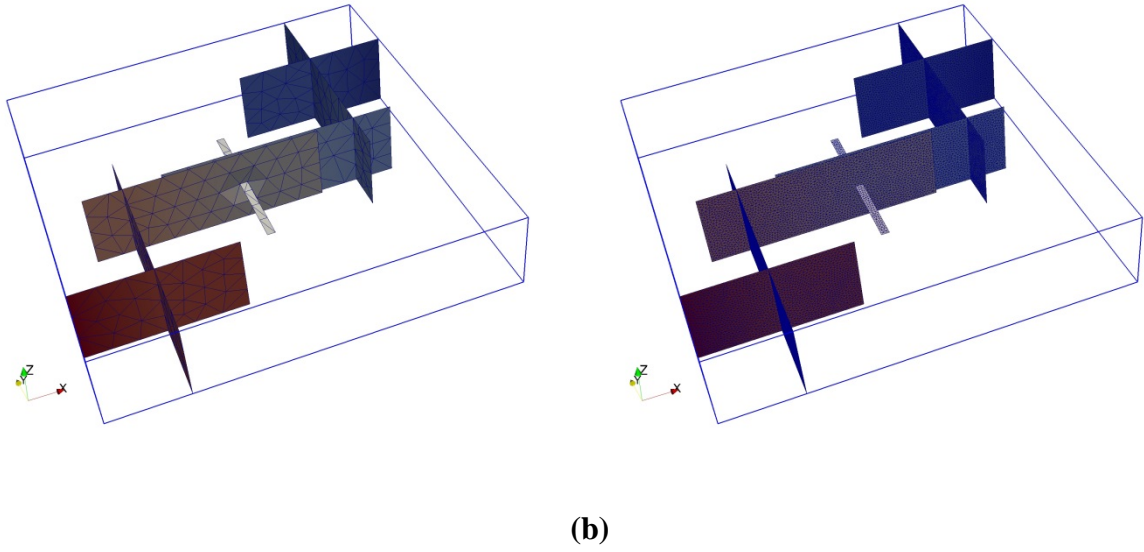
### 425 3.3. Poor-connected DFNs

426 In order to assess the capacity of the mesh generator to treat poorly connected DFNs, we  
 427 consider in this section a 7-fracture system located within a  $10m \times 10m \times 2m$  block (Fig. 11).



428 Fig. 11. 7-fracture DFN including two sets of vertical fractures, the first set including the  
 429 fractures  $\mathcal{F}_1, \mathcal{F}_2, \mathcal{F}_3$  and the second one including  $\mathcal{F}_5, \mathcal{F}_6, \mathcal{F}_7$ , which are related by a  
 430 horizontal fracture  $\mathcal{F}_4$ . All vertical fractures are completed throughout the block and the  
 431 network is symmetric with respect to the center of DFN block. The intersection  
 432 between  $\mathcal{F}_4$  and two parallel fractures  $\mathcal{F}_3$  and  $\mathcal{F}_5$  creates an extremely small feature  $\varepsilon$ . The  
 433 DFN is shown in top-down view (a) and 3D view (b).

434 The DFN involves two separated sets of vertical fractures related by the horizontal one  $F_4$  .  
435 The intersections between  $F_4$  with two parallel fractures  $F_3$  and  $F_5$  result in an extremely  
436 small sub-fracture of width  $\varepsilon$ . As discussed above in Section 0, the appearance of tiny sub-  
437 fractures created by the intersection between fractures could yield to poor quality mesh cell in  
438 the resulting mesh. A well-known solution for this issue is to reduce the discretization size to  
439 the size of the small sub-fracture or to use adaptive meshes. In this configuration, it means  
440 that  $h$  has to be less than  $\varepsilon$  leading to the increase of the total mesh cell number. Another  
441 solution to circumvent this issue is to remove  $F_4$  from the network as proposed by several  
442 DFN mesh approaches, for instance the FRAM method (Hyman et al., 2014). However,  
443 removing the fracture  $F_4$  will obviously lead to the loss of global connectivity of the network  
444 along the horizontal directions. As an extreme example considering this fracture network  
445 without  $F_4$ , the effective permeabilities along x- and y-axis of the DFN will be equal to zero.  
446 Using FraC approach and its flexible strategy for intersection point treatment, the intersection  
447 between  $F_4$  and  $F_3$ ,  $F_5$  can be accounted for into coarse meshes without using a lower  
448 discretization for  $F_4$  and without affecting the global mesh quality and DFN connectivity.  
449  
450 Fig. 12 illustrates an example of a coarse mesh (Fig. 12a) and a fine mesh (Fig. 12b) for the 7-  
451 fracture DFN created using FraC. For both cases  $h$  is the same for all fractures. Obviously, as  
452 the tiny fracture width is smaller than  $h$  in the coarse mesh, the triangulation of this fracture  
453 leads to non-equilateral triangles. Moreover, we can easily notice from Fig. 12a the  
454 displacement of the intersection point between  $F_4$  and  $F_3$  to the location of the one between  
455  $F_4$  and  $F_5$  .  
456



457 *Fig. 12. Meshes for the 7-fracture DFN built obtained through the FraC approach. The issue*  
 458 *of tiny sub-fracture created by the intersections between  $F_4$  and  $F_3$ ,  $F_5$  is solved by either*  
 459 *applying the AoM approach to the coarse mesh (456 cells) (a) or reducing the mesh size*  
 460 *which leads to a fine mesh (25 671 cells) (b).*

461 Qualitatively speaking, the Fig. 12a also reveals the good quality of the mesh cells around this  
 462 location. To assess the influence of the minor change in DFN geometry, we compare  
 463 numerical result of steady-state single-phase flow within both the coarse and fine meshes. The  
 464 DFN is assumed to be homogeneous with the isotropic permeability of the fractures  
 465  $k_f = 10^{-11} \text{ m}^2$  and the fracture aperture of  $b = 10^{-2} \text{ m}$ .

466 Table 1 shows the numerical effective permeabilities along three original directions:  $\bar{k}_{\alpha,f}$   
 467 computed from steady-state flow simulations on the fine mesh and  $\bar{k}_{\alpha,c}$  from the coarse mesh  
 468 with  $\alpha \in \{x, y, z\}$ .

469

470

	Fine mesh		Coarse mesh	
	$\bar{k}_{\alpha,f}$ [ $10^{-15}$ m <sup>2</sup> ]	CPU time [s]	$\bar{k}_{\alpha,c}$ [ $10^{-15}$ m <sup>2</sup> ]	CPU time [s]
x-direction	55.6	7.4	60.0	0.15
y-direction	55.6	7.5	60.0	0.15
z-direction	320.0	7.0	320.0	0.13

471 *Table 1. Effective permeabilities along three original principal directions:  $\bar{k}_{\alpha,f}$  computed*  
472 *from steady-state flow simulations on the fine mesh and  $\bar{k}_{\alpha,c}$  from the coarse mesh.*

473

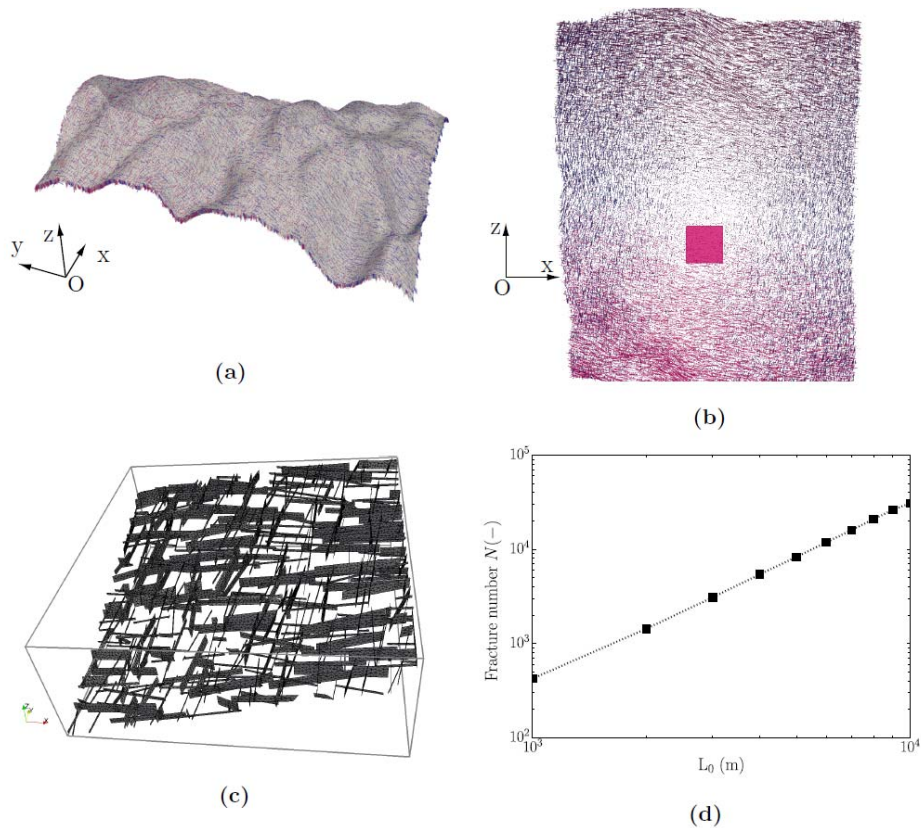
474 It is noticeable that (i) the geometric similarity of the network along  $x$  and  $y$  directions leading  
475 to the equality between the effective permeabilities along these axis,  $\bar{k}_x = \bar{k}_y$  for both the fine  
476 and coarse simulations; and (ii) the effective permeabilities computed from the simulations on  
477 the coarse mesh are slightly higher than those obtained from those on the fine mesh but they  
478 are of the same order of magnitude.

479 This discrepancy is due to the change of intersection location between the related fracture and  
480 the others ones. In addition, the geometry has been slightly changed compared to the original  
481 structure. Furthermore, the effective permeability along  $z$ -axis of both the fine and coarse  
482 meshes matches correctly, about  $3.2 \times 10^{-13}$  m<sup>2</sup>. It is noteworthy that the fracture  $F_4$  spreads  
483 horizontally and therefore its influence on the vertical effective conductivity is negligible.  
484 Table 1 also emphasizes the speed-up in CPU time for flow simulations when using the coarse  
485 mesh instead of the fine mesh with a speed-up factor of 50.

#### 486 **4. Scalability of the mesh generator**

487 The scalability of the meshing algorithms is now investigated, based on the result of  
488 mesh generations of the benchmark 33-fracture and the Bloemendaal's DFN (Verscheure et  
489 al., 2012) using the AoM approach and the open source software Dumux. The latter DFN is a

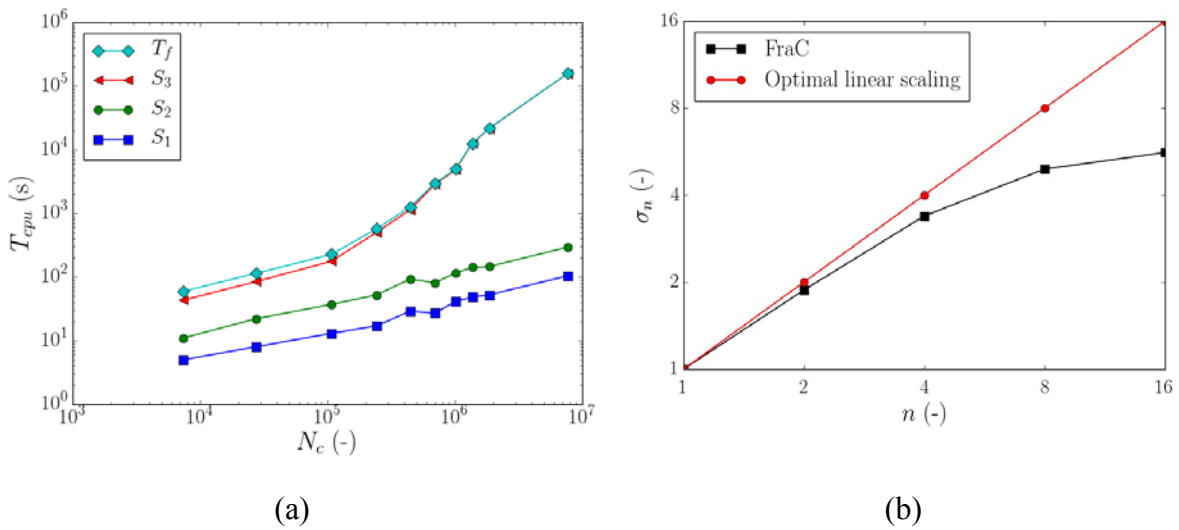
490 semi-synthetic DFN where the network's properties are closely based on the geological data  
 491 from the fictitious but realistic Bloemendaal reservoir. The semi-synthetic DFN consists of  
 492 more than 50,000 rectangular-shaped fractures that lie on a domain of  $12 \text{ km} \times 15 \text{ km} \times 1.4$   
 493 km. The thickness of the flowing zone is about 200 m (Fig. 13a,b) while the mean reservoir  
 494 thickness equals 10 m.



495  
 496 *Fig. 13. Semi-synthetic Bloemendaal fracture network in lateral view (a) and in top-down*  
 497 *view (b). Only the region inside the red box in (b) will be meshed. An example of resulting*  
 498 *mesh for the case  $L_0 = 1 \text{ km}$  where the DFN consists of around  $5 \times 10^2$  fractures is shown in*  
 499 *(c), and (d) reports variation of fracture number  $N$  in the bounding box (in red) w.r.t. the box*  
 500 *size  $L_0$ .*

501  
 502 Simulations using the DFN don't model the whole fracture network at the reservoir scale.  
 503 Classically, well-tests, flow-meters or interference tests, consider an influence zone of a few

504 kilometers around the wells (FracFlow 2017, Bourbiaux et al., 2002). Therefore, only  
505 fractures inside a bounding box of  $L_0 \times L_0 \times 1.4$  km (red box, Fig. 13b) are taken into account.  
506 The bounding box length  $L_0$  initially equals to 1 km, the associated DFN contains around  $5 \times$   
507  $10^2$  fractures (Fig. 13c). The DFN under consideration is expanded by increasing  $L_0$  up to ten  
508 kilometers. Fig. 13d displays a log-log graph of the variation of the fracture number  $N$  in the  
509 DFN bounding box with respect to  $L_0$  showing a  $N \sim L_0^2$  relationship. The unit mesh size  $h$   
510 remains constant for all meshing realizations resulting in progressively larger grids.  
511 On one hand, using the benchmark DFN the performance of the mesh generator on a constant  
512 DFN for different refinement levels is studied. On other hand, the Bloemendaal case is used to  
513 provide a sensitivity analysis of the FraC's performance considering statistical consistent  
514 DFNs of which the fracture number increase with space. Fig. 14a reports the variation of the  
515 elapsed time  $T_{S_i}$  required by the meshing step  $S_i$  with  $i = \overline{1,3}$  (cf. section 2.1) as well as the  
516 final wall-clock time  $T_f$  with respect to the mesh cell number  $N_c$ .

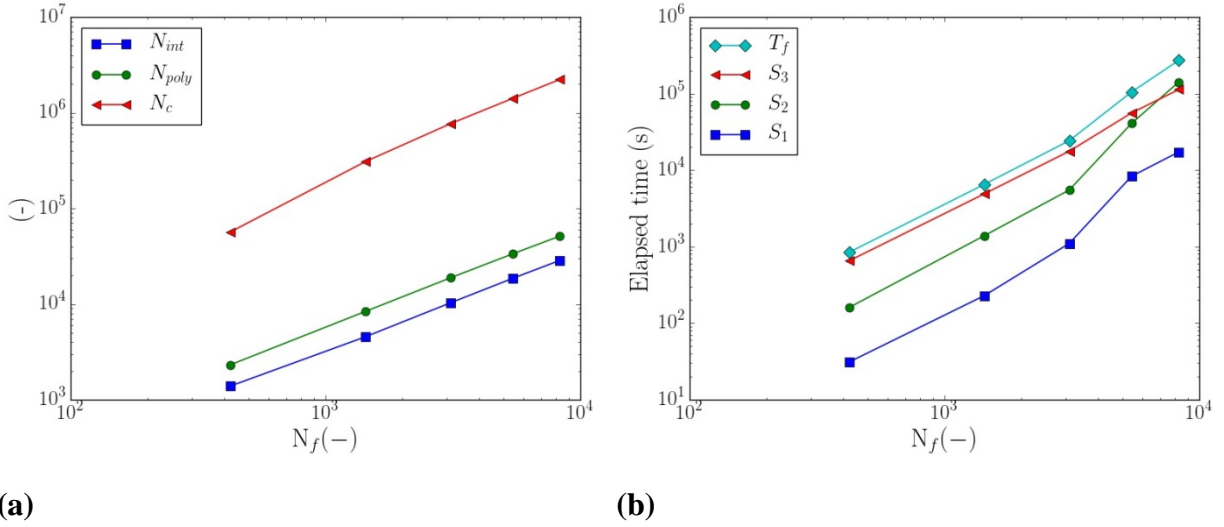


517 *Fig. 14. Benchmark 33-fracture DFN: Log-log relationship of the total elapsed time  $T_{cpu}$  and*  
518 *that required by each meshing step with respect to the grid cell number  $N_c$  (a), and speed-up*  
519 *ratio of parallel realizations of the mesh generation for the finest mesh ( $8 \times 10^6$  cells) (b).*

520 It can be noticed that the step  $S_3$  is the most expensive. It's remarkable that  $T_3$  is at least one  
521 order of magnitude higher than the two others ones for the meshes consisting of up to  $10^5$   
522 elements. This discrepancy in wall-clock time between the meshing steps could increase to 2  
523 or 3 orders of magnitude for the fine meshes. For  $N_c$  higher than  $10^5$ , the total computational  
524 time  $T_f$ , with a significant contribution from  $S_3$ , scales as  $N_c^{1.3}$ . It is noteworthy that the step  $S_3$   
525 can be run on several processors using the multiprocessing approach. The finest mesh (about  
526  $8 \times 10^6$  elements) is used for the parallel computing exercise. The Fig. 14b illustrates the  
527 scaling up ratio  $\sigma_n$  which is the ratio between  $T_1$  over  $T_n$ , elapsed time of 1 and  $n$  (CPUs). It  
528 is expected that this ratio increases linearly with  $n$ , that is unfortunately not the case in our  
529 exercise: it shows that the speeding up is fairly good with  $n$  is up to 4 processors, then it  
530 degrades quickly for higher CPU numbers. This can be explained by the fact that the  
531 workload is distributed to the processors by dividing the number of closed outline by the  $n$ ,  
532 the CPU number. This load balancing approach is simple to implement, however it leads to an  
533 load imbalance between different processors because of the difference between the fracture  
534 size. This could result in a nonlinear speeding up as observed in Fig. 14b.

535 Fig. 15a illustrates the variation of the number of fracture intersections  $N_{int}$ , the number of  
536 closed contours  $N_{poly}$  and the number of grid cells  $N_c$  over  $N_f$ , the fracture number within the  
537 Bloemendaal DFN. It shows a roughly linear relationship between  $N_{int}$ ,  $N_{poly}$  and  $N_c$  with  
538 respect to  $N_f$ . The execution times for meshing realizations are plotted in Fig. 15b, revealing  
539 that the mesh generation scales like  $N_f^{1.5}$ . Moreover, for large DFNs with up to  $10^4$  fractures,  
540 the execution times required by  $S_2$  and  $S_3$  are of same order of magnitude.

541



542 Fig. 15. Semi-synthetic DFN of the Bloemendaal reservoir: Log-log plot of the number of  
 543 fracture intersection  $N_{int}$ , the number of closed contours  $N_{poly}$  and the number of grid cells  $N_c$   
 544 with respect to the fracture number  $N_f$  (a); and log-log plot of the elapsed time versus  $N_f$  (b).  
 545

546 From these remarks, one can observe that the mesh generator is scalable for moderate  
 547 numbers of fractures and moderate number of intersections between fractures. However,  
 548 advance numerical approach to reduce execution time, e.g. local mesh refinement or parallel  
 549 computing, should be applied when working on large-scale densely-distributed DFNs.

## 550 5. Conclusions

551 In this paper, we have introduced a new conforming mesh method, so-called FraC, for  
 552 mesh generation of fracture networks. The cornerstone of the FraC approach is to decompose  
 553 each fracture into a set of connected closed contours, between which extended intersection  
 554 segments will be discretized in a conforming manner. Three strategies for intersecting points  
 555 are applied to ensure an acceptable quality of the final mesh. In light of the mesh quality  
 556 studies and mesh validations using steady-state flow simulations, the adaptive AoM strategy,  
 557 standing for Adding or Moving intersection points, proved its superiority against the two  
 558 others. The triangulation step of closed contours and the triangulated surfaces merging are

559 done using the LaGrit toolbox (Los Alamos Grid Toolbox, 2013). FraC is able to create good  
560 quality meshes for complex DFNs, even in case of large variation in size between intersecting  
561 fractures as shown in Section 3.3. Another important advantage is that flow, transport or other  
562 numerical simulations can be carried out on FraC meshes using classical numerical methods  
563 and software without any additional computational effort. For example, the “non-manifold”  
564 topology of resulting meshes may be handled by finite element codes (Cast3M (2017)) or  
565 finite volume codes like PFLOTRAN (Lichtner et al., 2013; Hammond et al., 2014; Hyman et  
566 al., 2014; Makedonska et al., 2015; Karra et al., 2015; Hyman et al., 2015) and DuMux  
567 (Flemisch et al., 2011; Ngo et al., 2017). In this work, for demonstration and validation  
568 purposes, steady state flow simulations have been carried out using both Cast3M and DuMux  
569 codes. Another application for transport simulations through DFNs can be found in Ngo et al.  
570 2017.

571 Ongoing works are about well test simulations and applications on the Bloemendaal reservoir  
572 where faults can act as barriers to fluid flow. In addition these faults are suspected to be  
573 longitudinal drains that can be modeled using related fractured fault. The analysis based on  
574 available data from two exploration wells emphasizes the flow barrier influences and have to  
575 be validated using numerical simulations.

576 In many cases, the matrix surrounding the fractures should be considered as sources that feed  
577 the fluid flow through the fractures and therefore should be accounted for. A possible solution  
578 is to mesh the matrix along with the fracture network (Ahmed et al., 2015, Brenner et al.,  
579 2015), however generating high-quality meshes for the fracture-matrix ensemble remains a  
580 great numerical challenge, especially for densely-distributed DFNs. It appears easier to  
581 perform simulations on fracture network meshes only and accounting for the matrix-fracture  
582 exchange via numerical or semi-analytical approximations. Such numerical techniques are the  
583 generalized dual-porosity (GDPM) method (Zyvoloski et al., 2008) or the Multiple

584 INteracting Continua (MINC) approach (De Dreuzy et al., 2013). The latter was initially  
585 developed in the late 1980s (e.g., Pruess and Narasimhan, 1985; Pruess et al., 1990) and  
586 improved more recently (e.g., Karimi-Fard et al., 2006; Tatomir et al., 2011; de Dreuzy et al.,  
587 2013). Semi-analytical approximations may also be used (Grenier et al., 2005; Painter et al.,  
588 2008; Noetinger, 2015). These approaches are useful because they allow to avoid challenging  
589 meshing issues. Nevertheless, it requires rigorous exercises for the validation of the matrix-  
590 fracture transfer formulations.

591 Finally, major issues are to model non-linear physical phenomena such as, multi-phase multi-  
592 component flow, sorption or reactive transport, up to hydromechanical coupling for the  
593 purpose of many applications.

594

## 595 **Acknowledgments**

596 The authors are grateful to IFPEN for funding the postdoctoral fellowship of T-D. Ngo. The  
597 authors would like to thank the Computational Earth Science Group of LANL for providing  
598 us the source code of LaGriT and dfnWorks. Finally, we thank anonymous reviewers for their  
599 valuable comments that help to improve the quality of this article.

600

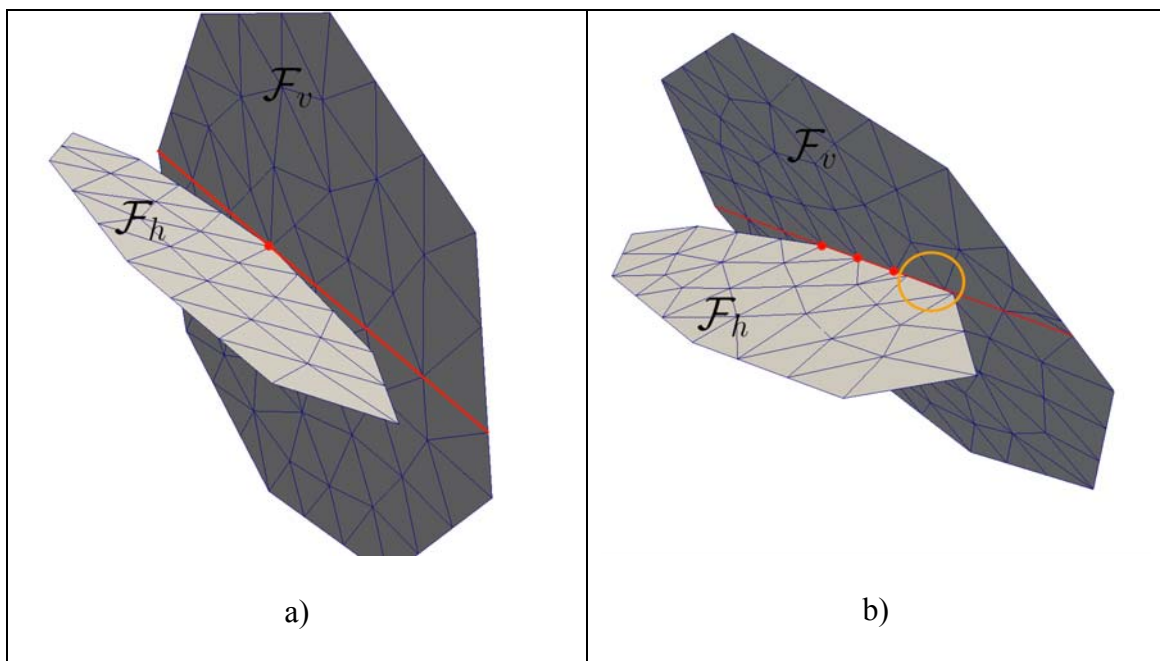
## 601 **Appendix A**

602 This appendix deals with meshing of fracture intersection configurations that may be  
603 encountered when using DFN modelling tools. A discussion given in the last point outlines  
604 the impact of the critical length for intersection point merging  $L_{\min}$ .

### 605 • **Meshing of complex two fracture configurations**

606 Degenerated configurations of a simple two-fracture DFN are first studied. A horizontal  
607 fracture ( $F_h$ ) and another vertical one ( $F_v$ ) are linked by only one point (Fig. A1a), and by

608 only one side (Fig. A1b) located on the perimeter of  $F_h$ . In both cases, the FraC meshing  
 609 procedure tends to divide  $F_v$  into two sub-fractures along the extended intersection line (in  
 610 red). The contour points of  $F_h$  inside the orange circle are very close but remain disconnected  
 611 from  $F_v$ . These examples show that in general the FraC approach is able to handle DFNs  
 612 containing bounded fractures, i.e. fractures that terminate into another one. However, it still  
 613 requires improvements to take into account other intricate cases, e.g. when the perimeter of a  
 614 fracture are in extremely close proximity to another fracture plane but these fractures stay  
 615 disconnected. For this purpose, a user-defined small parameter should be set for intersection  
 616 tests.



617 *Fig. A1. Degenerated configurations of a two-fracture DFN: the fractures are connected by*  
 618 *only one contour point (a) and by only one side (b).*

619

620 **• Multiple intersections**

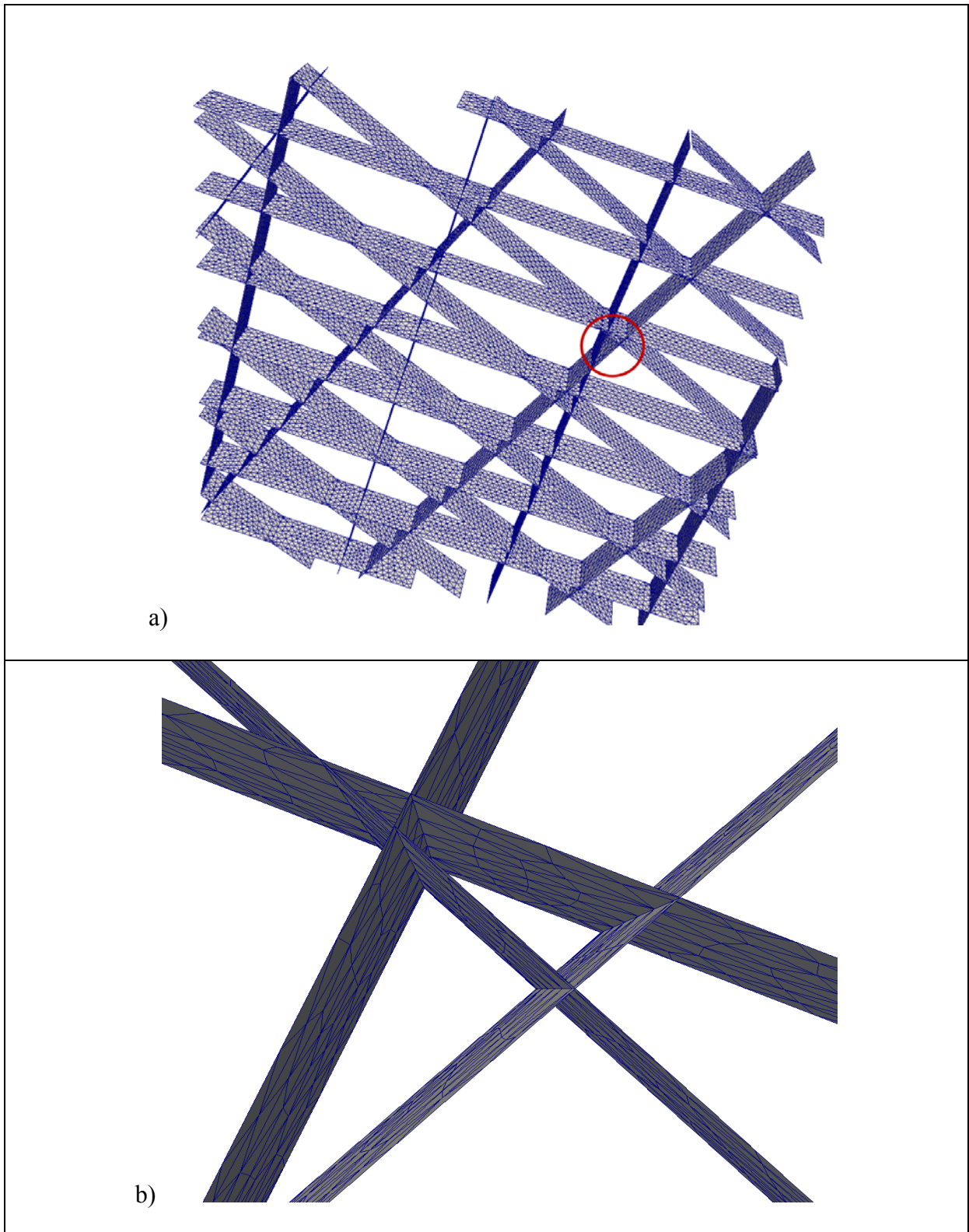
621 We explore now the MWR-DFN considered in Section 3.3. Three meshes are generated with  
 622  $h=1.4\text{m}$ ,  $h=3.5\text{m}$  and  $h=7\text{m}$ . Two  $L_{\min}$  values are chosen to assess the impact of this parameter

623 on the behavior of the mesh generator at multiple intersection locations (Fig. A2). The mesh  
624 shown in Fig. A2a is generated with  $h=1.4\text{m}$ . It is noticeable that whatever the  $L_{\min}$  value the  
625 DFN geometry inside the triple intersection area is correctly modeled (Fig. A2a and A2b).  
626 Since the selected discretization is fine enough, all the intersection points are added to the  
627 fracture contours.

628 The second discretization,  $h=3.5\text{m}$ , provides different results. For  $L_{\min}=0.01h$  the intersection  
629 area is explicitly modeled (Fig. A3b) without fracture deformation whereas with  $L_{\min}=0.2h$   
630 two intersection points are merged (Fig. A3c). The intersection segments are partially merged  
631 because the selected discretization is fine enough to partially model the intersection. The  $L_{\min}$   
632 criterion is fulfilled only for the red points in Fig. A3b, which are modeled by a single point in  
633 orange in Fig. A3c. The last discretization is obtained with  $h=7\text{m}$  (Fig. A4). For  $L_{\min}=0.01h$ ,  
634 the geometry of the area under study is correctly modeled, however the mesh cell size spans a  
635 wide range from about 2m inside the intersection area to 7m elsewhere (Fig. A4a,b). Finally,  
636 for  $L_{\min}=0.2h$ , the three intersection points are merged and the three intersection lines are  
637 modeled by a single segment (Fig. A4c).

638

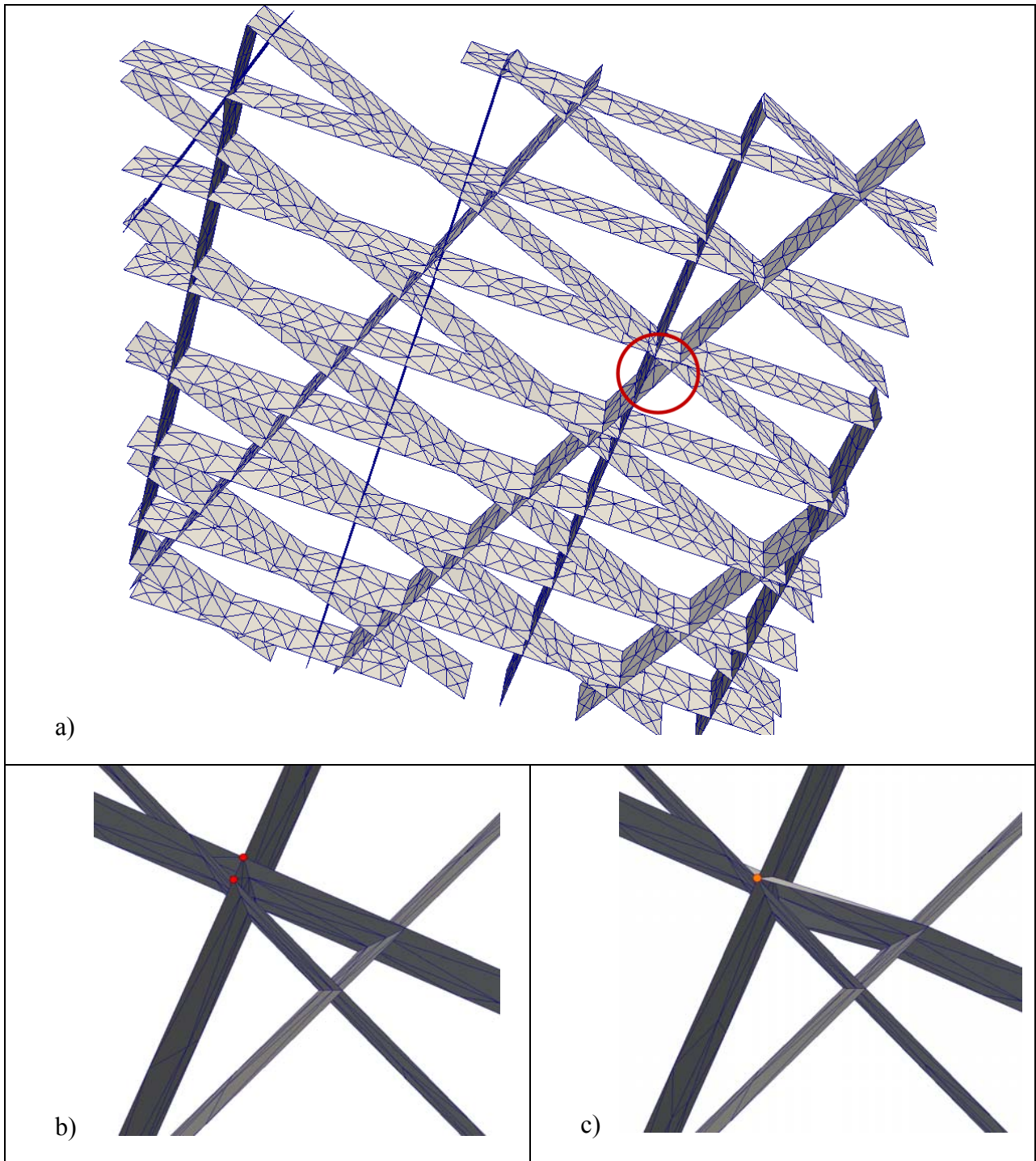
639



641 Fig. A2. a) Global view of the MWR-DFN mesh with  $h=1.4\text{m}$ ,  $L_{\min}=0.2h$ . Zoom on a triple

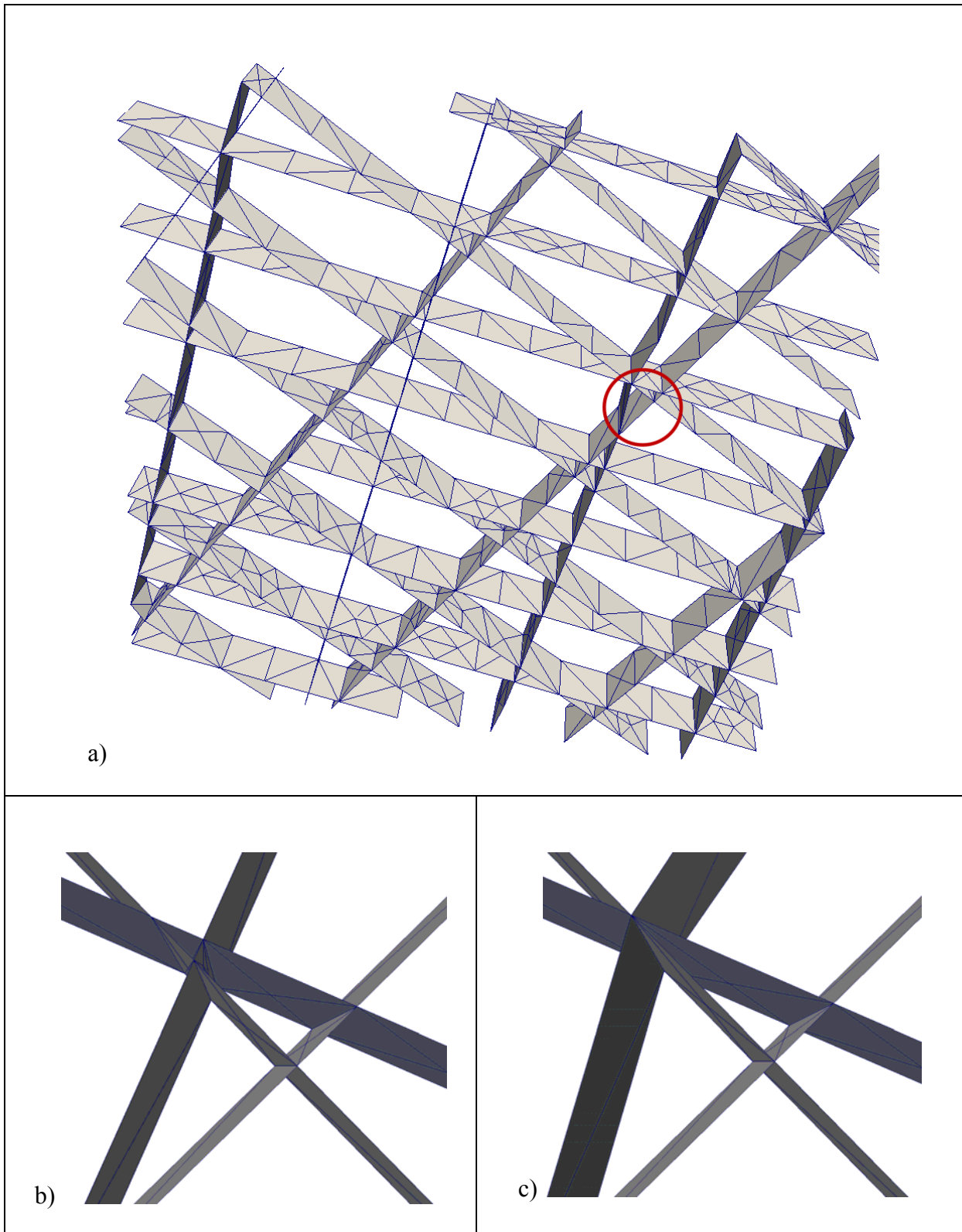
642 intersection location for  $L_{\min}=0.01h$  (b) and  $L_{\min}=0.2h$  (c).

643



645 Fig. A3. a) Global view of the MWR-DFN mesh with  $h=3.5\text{m}$ ,  $L_{\min}=0.2h$ . Zoom on a triple  
646 intersection location for  $L_{\min}=0.01h$  (b) and  $L_{\min}=0.2h$  (c).

647



649 Fig. A4. a) Global view of the MWR-DFN mesh with  $h=7.0\text{m}$ ,  $L_{\min}=0.2h$ . Zoom on a triple  
650 intersection location for  $L_{\min}=0.01h$  (b) and  $L_{\min}=0.2h$  (c).

651

652 **References**

653 Acuna, J. A., & Yortsos, Y. C. (1991, January). Numerical construction and flow simulation  
654 in networks of fractures using fractal geometry. In *SPE Annual Technical Conference and*  
655 *Exhibition*. Society of Petroleum Engineers.

656

657 Adler, P.M., Thovert J.F., Mourzenko V.V., 2012. Fractured porous media. Oxford University  
658 Press.

659

660 Ahmed, R., Edwards, M.G., Lamine, S., Huisman, B.A., Pal, M., 2015. Three-dimensional  
661 control-volume distributed multi-point flux approximation coupled with a lower-  
662 dimensional surface fracture model. *Journal of Computational Physics* 303, 470–497.

663

664 Aquilina, L., Rose, P., Vaute, L., Brach, M., Gentier, S., Jeannot, R., Jacquot, E., Audigane,  
665 P., Tran-Viet, T., Jung, R., et al., 1998. A tracer test at the Soultz-Sous-Forets Hot Dry  
666 Rock geothermal site, in: *Proceedings, Twenty-Third Workshop on Geothermal Reservoir*  
667 *Engineering*, Stanford University, Stanford, California, pp. 343–350.

668

669 Beicip-FranLab, 2017. FracaFlow. URL: <http://www.beicip.com/fractured-reservoirs>.

670

671 Benedetto, M.F., Berrone, S., Pieraccini, S., Scialò, S., 2014. The virtual element method for  
672 discrete fracture network simulations. *Computer Methods in Applied Mechanics and*  
673 *Engineering* 280, 135–156.

674

675 Benedetto, M.F., Berrone, S., Scialò, S., 2016. A globally conforming method for solving  
676 flow in discrete fracture networks using the virtual element method. *Finite Elements in*  
677 *Analysis and Design* 109, 23–36.

678

679 Berrone, S., Pieraccini, S., Scialò, S., 2013. A PDE-constrained optimization formulation for  
680 discrete fracture network flows. *SIAM Journal on Scientific Computing* 35(2), B487–  
681 B510.

682

683 Berrone, S., Pieraccini, S., Scialò, S., 2017. Non-stationary transport phenomena in networks  
684 of fractures: effective simulations and stochastic analysis. *Computer Methods in Applied*  
685 *Mechanics and Engineering* 315, 1098–1112.

686

687 Bodin, J., Porel, G., Delay, F., Ubertosi, F., Bernard, S., De Dreuzy, J.R., 2007. Simulation  
688 and analysis of solute transport in 2d fracture/pipe networks: The solfrac program. *Journal*  
689 *of Contaminant Hydrology* 89(1), 1–28.

690

691 Bourbiaux, B., 2010. Fractured reservoir simulation: A challenging and rewarding issue. *Oil*  
692 *& Gas Science and Technology–Revue de l’Institut Français du Pétrole* 65(2), 227–238.

693

694 Bourbiaux, B., Basquet, R., Cacas, M.C., Daniel, J.M., Sarda, S., et al., 2002. An integrated  
695 workflow to account for multi-scale fractures in reservoir simulation models:  
696 implementation and benefits, in: *Abu Dhabi International Petroleum Exhibition and*  
697 *Conference*, Society of Petroleum Engineers.

698

699 Borouchaki, H. and George, P.L., 1998. Delaunay triangulation and meshing. Application to  
700 finite elements. Herms, Paris.  
701

702 Botsch, M., Kobbelt, L.A., 2001. Robust Procedure to Eliminate Degenerate Faces from  
703 Triangle Meshes. In: Vision, Modeling & Visualization. 283-289.  
704

705 Brenner, K., Groza, M., Guichard, C., Masson, R., 2015. Vertex approximate gradient scheme  
706 for hybrid dimensional two-phase Darcy flows in fractured porous media. ESAIM:  
707 Mathematical Modelling and Numerical Analysis 49(2), 303–330.  
708

709 Cacas, M.C., Ledoux, E., de Marsily, G., Tillie, B., Barbreau, A., Durand, E., Feuga, B.,  
710 Peaudecerf, P., 1990. Modeling fracture flow with a stochastic discrete fracture network:  
711 calibration and validation: 1. The flow model. Water Resources Research 26(3), 479–489.  
712 URL: <http://dx.doi.org/10.1029/WR026i003p00479>, doi:10.1029/WR026i003p00479.  
713

714 Cast3M, 2017. Website for the computer code cast3m. URL: <http://www.cast3m.cea.fr>.  
715

716 De Dreuzy, J.R., Pichot, G., Poirriez, B., Erhel, J., 2013. Synthetic benchmark for modeling  
717 flow in 3D fractured media. Computers & Geosciences 50, 59–71.  
718

719 De Dreuzy, J.R., Rapaport, A., Babey, T., Harmand, J., 2013. Influence of porosity structures  
720 on mixing-induced reactivity at chemical equilibrium in mobile/immobile Multi-Rate Mass  
721 Transfer (MRMT) and Multiple INteracting Continua (MINC) models. Water Resour. Res.  
722 49 (12), 8511–8530.  
723

724 Delaunay, B., 1934. Sur la sphère vide. A la mémoire de Georges Voronoï. Bulletin de  
725 l'Académie des Sciences de l'URSS. Classe des sciences mathématiques et na, no. 6, 793–  
726 800  
727

728 Delorme, M., Bossie-Codreanu, D., Ben-Gharbia, I., Khebzegga, O., Khvoenkova, N., Ricois,  
729 O., 2016. Unconventional production forecast needs integration of field hydraulic  
730 stimulation data through fracture model calibration and optimized numerical scheme, in:  
731 SPE Argentina Exploration and Production of Unconventional Resources Symposium,  
732 Society of Petroleum Engineers, SPE-180946-MS.  
733

734 Dershowitz, W., Fidelibus, C., 1999. Derivation of equivalent pipe network analogues for  
735 three-dimensional discrete fracture networks by the boundary element method. Water  
736 Resources Research 35(9), 2685–2691.  
737

738 DuMux, 2017. Web site for the computer code DuMux. URL: <http://www.dumux.org/>.  
739

740 Erhel, J., De Dreuzy, J.R., Poirriez, B., 2009. Flow simulation in three-dimensional discrete  
741 fracture networks. SIAM Journal on Scientific Computing 31(4), 2688–2705.  
742

743 Flemisch, B., Darcis, M., Erbertseder, K., Faigle, B., Lauser, A., Mosthaf, K., Müthing, S.,  
744 Nuske, P., Tatomir, A., Wolff, M., et al., 2011. Dumux: DUNE for multi-{phase,  
745 component, scale, physics,...} flow and transport in porous media. Advances in Water  
746 Resources 34(9), 1102–1112.  
747

748 Fournou, A., Benabderrahmane, H., Grenier, C., Delay, F., 2007. Development and  
749 qualification of a smeared fracture modelling approach for transfers in fractured media, in:  
750 Groundwater in Fractured Rocks: IAH Selected Paper Series, volume 9. Taylor & Francis,  
751 pp. 587–603.

752

753 Fournou, A., Grenier, C., Benabderrahmane, A., Delay, F., 2013. A continuum voxel approach  
754 to model flow in 3d fault networks: A new way to obtain up-scaled hydraulic conductivity  
755 tensors of grid cells. *Journal of Hydrology* 493, 68–80.

756

757 Fournou, A., Noetinger, B., Borderie, C., 2016. An original and useful approach to mesh a  
758 discrete fracture network using a Delaunay triangulation: Application on flow and  
759 transport upscaling from characterization scale to reservoir scale, in: *Computational*  
760 *Methods in Water Resources Conference 2016, XXI International Conference*, pp. 36–36.

761

762 Frey, P.J., George, P. L., 2000. *Mesh generation: application to finite elements* (p. 816). Paris:  
763 Hermes Science.

764

765 Grenier, C., Fournou, A., Mouche, E., Delay, F., Benabderrahmane, H., 2005. Assessment of  
766 Retention Processes for Transport in a Fractured System at Äspö (Sweden) Granitic Site:  
767 from Short-Time Experiments to Long-Time Predictive Models. *Dynamics of Fluids and*  
768 *Transport in Fractured Rock* , 117–128.

769

770 Gylling, B., Moreno, L., Neretnieks, I., 1999. The channel network model—a tool for  
771 transport simulations in fractured media. *Groundwater* 37(3), 367–375.

772

773 Hammond, G.E., Lichtner, P.C., Mills, R.T., 2014. Evaluating the performance of parallel  
774 subsurface simulators: An illustrative example with PFLOTRAN. *Water Resources*  
775 *Research* 50(1), 208–228.

776

777 Huang, N., Jiang, Y., Li, B., Liu, R., 2016. A numerical method for simulating fluid flow  
778 through 3-d fracture networks. *Journal of Natural Gas Science and Engineering* 33, 1271–  
779 1281.

780

781 Huber, R., Helmig, R., 2000. Node-centered finite volume discretizations for the numerical  
782 simulation of multiphase flow in heterogeneous porous media. *Computational Geosciences*  
783 4(2), 141–164.

784

785 Hyman, J.D., Gable, C.W., Painter, S.L., Makedonska, N., 2014. Conforming Delaunay  
786 triangulation of stochastically generated three dimensional discrete fracture networks: a  
787 feature rejection algorithm for meshing strategy. *SIAM Journal on Scientific Computing*  
788 36(4), A1871–A1894.

789

790 Hyman, J.D., Karra, S., Makedonska, N., Gable, C.W., Painter, S.L., Viswanathan, H.S.,  
791 2015. dfnWorks: A discrete fracture network framework for modeling subsurface flow and  
792 transport. *Computers & Geosciences* 84, 10–19.

793

794 Jourdain, X., Colliat, J.B., De Sa, C., Benboudjema, F., Gatuingt, F., 2014. Upscaling  
795 permeability for fractured concrete: meso–macro numerical approach coupled to strong  
796 discontinuities. *International Journal for Numerical and Analytical Methods in*  
797 *Geomechanics* 38(5), 536–550.

798

799 Karimi-Fard, M., Gong, B., Durlofsky, L.J., 2006. Generation of coarse-scale continuum flow  
800 models from detailed fracture characterizations. *Water resources research* 42(10).

801

802 Karra, S., Makedonska, N., Viswanathan, H.S., Painter, S.L., Hyman, J.D., 2015. Effect of  
803 advective flow in fractures and matrix diffusion on natural gas production. *Water*  
804 *Resources Research* 51(10), 8646–8657.

805

806 Khvoenkova, N., Delorme, M., 2011. An optimal method to model transient flows in 3D  
807 discrete fracture network, in: IAMG conference, pp. 1238–1249.

808

809 Lichtner, P.C., Hammond, G.E., Lu, C., Karra, S., Bisht, G., Andre, B., Mills, R.T., Kumar,  
810 J., 2013. PFLOTRAN User Manual. Technical Report.

811

812 Long, J., Remer, J., Wilson, C., Witherspoon, P., 1982. Porous media equivalents for  
813 networks of discontinuous fractures. *Water Resources Research* 18(3), 645–658.

814

815 Los Alamos Grid Toolbox, 2013. Los Alamos National Laboratory. URL:  
816 <http://lagrit.lanl.gov>.

817

818 Makedonska, N., Painter, S.L.L., Bui, Q.M., Gable, C.W., Karra, S., 2015. Particle tracking  
819 approach for transport in three-dimensional discrete fracture networks. *Computational*  
820 *Geosciences* 19(5), 1123–1137.

821

822 Matthai, S.K., Nick, H.M., 2009. Upscaling two-phase flow in naturally fractured reservoirs.  
823 AAPG bulletin 93(11), 1621–1632.  
824

825 Miller, G.L., Talmor, D., Teng, S-H., and Walkington, N., 1995. A Delaunay Based  
826 Numerical Method for Three Dimensions: Generation, Formulation, and Partition.  
827 Proceedings of the Twenty-Seventh Annual ACM Symposium on the Theory of  
828 Computing.  
829

830 Mustapha, H., and Dimitrakopoulos, R. (2011). Discretizing two-dimensional complex  
831 fractured fields for incompressible two-phase flow. *International Journal for Numerical*  
832 *Methods in Fluids*, 65(7), 764-780.  
833

834 Murphy, M., Mount, D.M., Gable, C.W., 2001. A point-placement strategy for conforming  
835 Delaunay tetrahedralization. *International Journal of Computational Geometry &*  
836 *Applications* 11(6), 669–682.  
837

838 Neuman, S., 1988. A proposed conceptual framework and methodology for investigating flow  
839 and transport in Swedish crystalline rocks. SKB Swedish Nuclear Fuel and Waste  
840 Management Co., Stockholm, September, Arbetsrapport , 88–37.  
841

842 Ngo, T. D., Fournon, A., Noetinger, B., 2017. Modeling of transport processes through large-  
843 scale discrete fracture networks using conforming meshes and open-source software.  
844 *Journal of Hydrology* 254, 66–79.  
845

846 Noetinger, B., 2015. A quasi steady state method for solving transient Darcy flow in complex  
847 3D fractured networks accounting for matrix to fracture flow. *Journal of Computational*  
848 *Physics* 283, 205–223.

849

850 Noetinger, B., Jarrige, N., 2012. A quasi steady state method for solving transient Darcy flow  
851 in complex 3D fractured networks. *Journal of Computational Physics* 231(1), 23–38.

852

853 Oda, M., 1985. Permeability tensor for discontinuous rock masses. *Geotechnique* 35, 483-  
854 495.

855

856 Pichot, G., Erhel, J., De Dreuzy, J.R., 2010. A mixed hybrid mortar method for solving flow  
857 in discrete fracture networks. *Applicable Analysis* 89(10), 1629–1643.

858

859 Pichot, G., Erhel, J., de Dreuzy, J.R., 2012. A generalized mixed hybrid mortar method for  
860 solving flow in stochastic discrete fracture networks. *SIAM Journal on scientific*  
861 *computing* 34(1), B86–B105.

862

863 Pruess, K., Narasimhan, T.N., 1985. A practical method for modeling fluid and heat flow in  
864 fractured porous media. *SPE J.* 25 (1), 14–26.

865

866 Pruess, K., Wang, J.S.Y., Tsang, Y.W., 1990. On thermohydrologic conditions near high-  
867 level nuclear wastes emplaced in partially saturated fractured tuff. 2- Effective continuum  
868 approximation. *Water Resour. Res.* 26 (6), 1249–1261.

869

870 Ricois, O., Gratien, J-M., Bossie Codreanu, D., Khvoenkova N., Delorme M., 2016.  
871 Advantages of an unstructured unconventional fractured media model integrated within a  
872 multiphysics computational platform, International Petroleum Technology Conference,  
873 IPTC-18846-MS.

874

875 Sander, O., Koch, T., Schröder, N., Flemisch, B., 2015. The Dune FoamGrid implementation  
876 for surface and network grids. CoRR abs/1511.03415. URL:  
877 <http://arxiv.org/abs/1511.03415>.

878

879 Jonathan R. Shewchuk. Delaunay refinement mesh generation. PhD–Thesis, Carnegie Mellon  
880 University, Pittsburg, 1997

881

882 Svensson, U., 2001. A continuum representation of fracture networks. Part I: Method and  
883 basic test cases. Journal of Hydrology 250(1), 170–186.

884

885 Painter, S. , Cvetkovic, V., Mancillas, J., Pensado, O., 2008. Time domain particle tracking  
886 methods for simulating transport with retention and first-order transformation, Water  
887 Resource Researches., 44(1).

888

889 Tatomir, A.B., Szykiewicz, A., Class, H., Helming, R., 2011. Modeling two phase flow in  
890 large scale fractured porous media with an extended multiple interacting continua. CMES  
891 77 (2), 81–112.

892

893 Verscheure, M., Fournon, A., Chilès, J.P., 2012. Joint inversion of fracture model properties  
894 for CO<sub>2</sub> storage monitoring or oil recovery history matching. *Oil & Gas Science and*  
895 *Technology–Revue d'IFP Energies nouvelles* 67(2), 221–235.

896

897 Warren, J.E., Root, P.J., 1963. The behavior of naturally fractured reservoirs, *SPE J.* 3 (3),  
898 245-255.

899

900 Zimmerman, R., Bodvarsson, G., 1996. Effective transmissivity of two-dimensional fracture  
901 networks, in: *International Journal of Rock Mechanics and Mining Sciences &*  
902 *Geomechanics Abstracts* 33, 433–438.

903

904 Zyvoloski, G. A. , Robinson, B. A., and Viswanathan, H. S., 2008. Generalized dual porosity:  
905 A numerical method for representing spatially variable sub-grid scale processes, *Advances*  
906 *in Water Resources* 31, 535–544.